FIB-TEM analysis of cometary material in 10 Stardust foil craters

Brendan A. HAAS [1,2,*], Christine FLOSS[1,2], Rhonda M. STROUD [3], and Ryan C. OGLIORE [1,2]

[1]Laboratory for Space Sciences, Washington University, St. Louis, Missouri 63130, USA
[2]Physics Department, Washington University, St. Louis, Missouri 63130, USA
[3]Materials Science and Technology Division, Naval Research Laboratory, 4555 Overlook Ave. SW, Washington, District of Columbia 20375, USA
[*]Corresponding author. E-mail: bahaas@wustl.edu

Abstract–Aluminum foils from the Stardust cometary dust collector contain impact craters formed during the spacecraft's encounter with comet 81P/Wild 2 and retain residues that are among the few unambiguously cometary samples available for laboratory study. Our study investigates four micron-scale (1.8–5.2 μm) and six submicron (220–380 nm) diameter craters to better characterize the fine (<1 μm) component of comet Wild 2. We perform initial crater identification with scanning electron microscopy, prepare the samples for further analysis with a focused ion beam, and analyze the cross sections of the impact craters with transmission electron microscopy (TEM). All of the craters are dominated by combinations of silicate and iron sulfide residues. Two micron-scale craters had subregions that are consistent with spinel and taenite impactors, indicating that the micron-scale craters have a refractory component. Four submicron craters contained amorphous residue layers composed of silicate and sulfide impactors. The lack of refractory materials in the submicron craters suggests that refractory material abundances may differentiate Wild 2 dust on the scale of several hundred nanometers from larger particles on the scale of a micron. The submicron craters are enriched in moderately volatile elements (S, Zn) when normalized to Si and CI chondrite abundances, suggesting that, if these craters are representative of the Wild 2 fine component, the Wild 2 fines were not formed by high-temperature condensation. This distinguishes the comet's fine component from the large terminal particles in Stardust aerogel tracks which mostly formed in high-temperature events.

INTRODUCTION

NASA's Stardust spacecraft encountered comet 81P/Wild 2 on January 2, 2004, successfully captured rocky particulate coma samples, and returned them to Earth on January 15, 2006 (Brownlee et al. 2006). Material returned by the Stardust mission constitutes our only unambiguously cometary material available for laboratory study, and thus continues to be critical to our characterization of outer solar system material (Zolensky et al. 2008).

Wild 2 is believed to be an ancient object whose orbit was perturbed by Jupiter and brought into the inner solar system in 1974 (Brownlee et al. 2006). Wild 2 had made five passages past its new perihelion distance of 1.58 AU at the time of Stardust's flyby (Tsou et al. 2004). During its passages through the inner solar system, the comet had dozens of jets of gas and dust originating from subsurface regions that contribute to the formation of the comet's coma (Brownlee et al. 2004).

Although the Stardust spacecraft successfully collected materials from Wild 2's coma, the encounter's relative speed of 6.12 km s^{-1} resulted in significant alteration to the cometary material. The Stardust sample collector used two separate media to capture impacting cometary material (1) ultra-low-density silica aerogel tiles and (2) aluminum foils covering the scaffolding surrounding the aerogel tiles. The types of impact processing the samples experienced were different in the two media (Kearsley et al. 2008).

The aerogel tiles effectively decelerated and captured many intact coarse (>1 μm) coma particles (Zolensky et al. 2008). Many of the fine (<1 μm) grains collected in the aerogel tiles were initially components of larger aggregate impactors that disaggregated and spread across millimeter-scale bulbous impact features (Burchell et al. 2008).

Investigations of the fine grains captured in aerogel have shown a variety of results. Submicron particles from aerogel track 80 had solar abundances of Fe, Mg, and S when averaged together, but individually had a wide range of compositions, suggesting that the fine grains are consistent with thermally unprocessed primordial dust close to solar composition (Stodolna et al. 2012). Grains smaller than 2 μm in size have a wide range of O isotopic compositions, indicating that Wild 2 fine grains are either a diverse sampling of inner solar system reservoirs or ancient outer-nebula dust (Ogliore et al. 2015). These results have differed from studies of coarse Wild 2 materials that frequently have high-temperature origins and volatile element depletions, and appear to have formed far from where comet Wild 2 accreted (Brownlee et al. 2012). The source of the Wild 2 fines could be determined through comparison of the Wild 2 fine volatile components with solar compositions. Materials formed in the inner solar system would be depleted in volatiles relative to CI chondrites, whereas materials inherited from the solar system's parent molecular cloud would not (Ogliore et al. 2015). However, the dispersion of fine grains across bulbous impact features in the aerogel tiles, as well as their intermixing with the aerogel, makes bulk elemental analysis of the fines difficult in that medium.

The aluminum foils on the sample collector allow us to directly study the fine-grained impactors. The foils were heavily cratered by submicron craters (Kearsley et al. 2008; Price et al. 2010), and slightly larger micron-scale craters (1–6 μm) are predominantly the result of aggregate impactors composed of submicron aggregate grains (Hörz et al. 2006). Cometary material in the foils is concentrated in residues located in the crater bottoms and sidewalls and thus is more localized than in the aerogel tracks. Surviving crystalline material has been found in a number of Stardust foil craters (Leroux et al. 2008a, 2010; Stroud et al. 2010) that analog studies indicate are surviving cometary grains rather than recrystallizations (Wozniakiewicz et al. 2012a). Analog foil studies have also shown that smaller impactors typically experience less alteration during the capture process (Croat et al. 2015) and as a result are less likely to have experienced conditions that could result in the loss of volatiles present in the impactors. The micron-scale (1–6 μm) and submicron (<1 μm) diameter craters on the Stardust aluminum foils are thus a promising source of information regarding comet Wild 2's fine grain component and can help constrain the volatile component and the source of the Wild 2 fines.

Studying submicron impactors in the Stardust foils provides the unique ability to directly analyze Wild 2's fine component. However, few attempts have been made to characterize micron-scale (Leroux et al. 2008a) and submicron craters (Leroux et al. 2010; Stroud et al. 2010) from the Stardust cometary foils. In this report, we aim to characterize the cometary residue present in four micron-scale craters (referenced as M1–M4) located on Stardust foils C2113N-B and C2118N-B as well as six submicron craters (referenced as SM5–SM10) located on Stardust cometary foil C2113N-A. Our micron-scale craters' diameters range from 1.8 to 5.2 μm (measured from the midpoints of the crater rims), corresponding to impactor sizes ranging from roughly 1.1 to 3.2 μm (Price et al. 2010). Our submicron craters' diameters range from 220 to 380 nm, corresponding to impactor sizes ranging from roughly 110–240 nm in diameter (Price et al. 2010). These results constitute some of the smallest Stardust foil impactors investigated to date and present new insight into the fine component of comet Wild 2.

SAMPLES AND METHODS

Initial identification of crater candidates and preliminary elemental characterization of these candidates were performed with scanning electron microscopy (SEM) and energy dispersive X-ray spectroscopy (EDS) methods, respectively. We captured secondary electron images covering the full surfaces of Stardust foils C2113N-B and C2118N-B using Washington University's Tescan Mira3 FE-SEM operated at 5 kV, locating two micron-scale crater candidates on each foil (Fig. 1). Identification of the micron-scale craters was performed with similar techniques. We acquired secondary electron images across a 5.28 mm² subsection of Stardust foil C2113N-A using Washington University's Tescan Mira3 FE-SEM operated at 1 kV, locating 20 crater candidates with diameters <0.5 μm.

We performed qualitative SEM-EDS analyses on the located craters with Washington University's JEOL JSM-840A SEM operated at 10 kV with an attached ThermoNoran System Six EDS system, in order to identify potential cometary material in the crater residues. Each micron-scale crater (M1–M4) returned measurable Si, Mg, Fe, and S signals, with one crater returning Ca signals as well (Table 1). Ten of the submicron craters returned measurable Si, Fe, S, or Ca signals. Mg was not observed; however, this was likely due to the Mg peak being overwhelmed by the adjacent
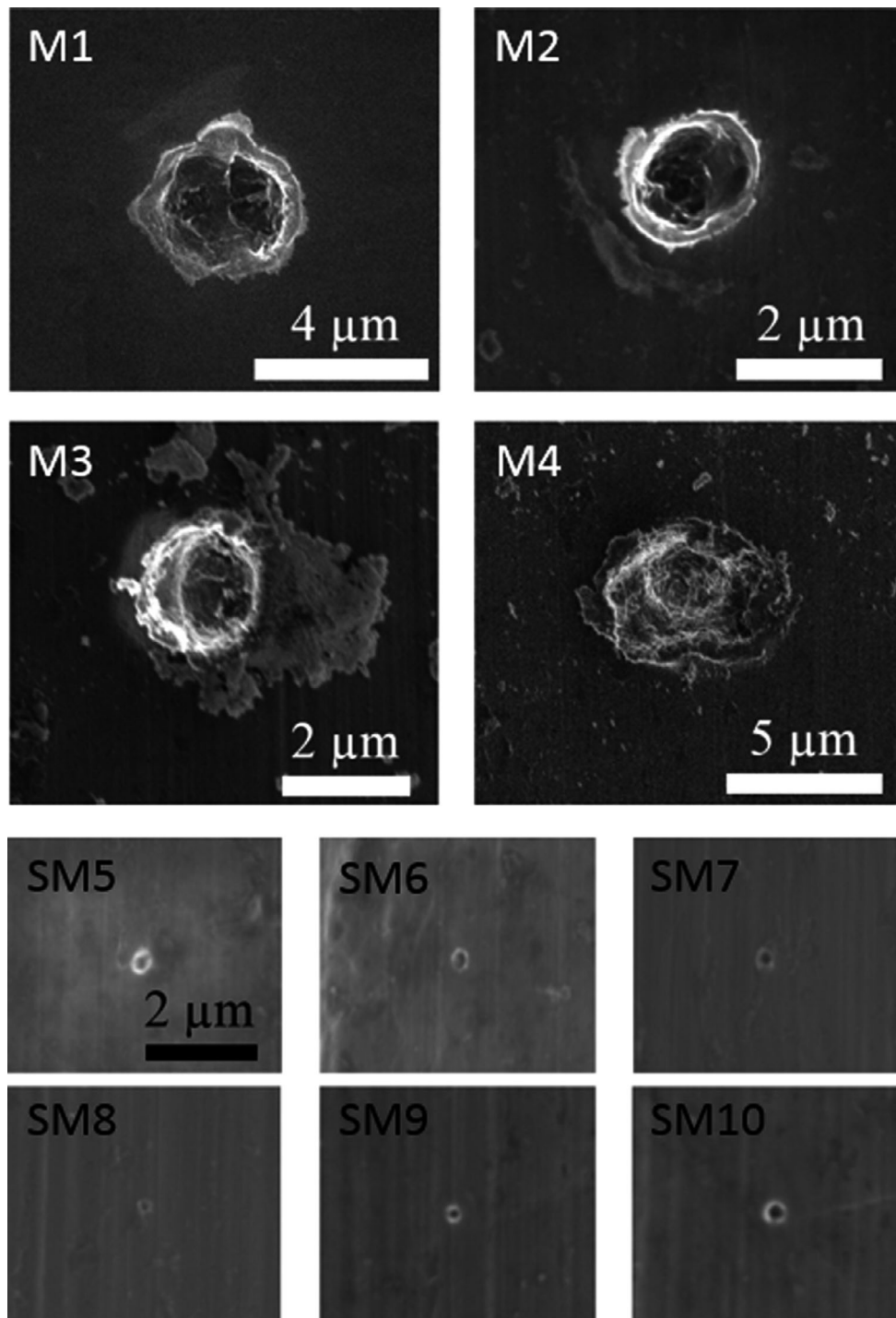
Fig. 1. Secondary electron images of micron-scale craters 1–4 (M1–M4) and submicron craters 5–10 (SM5–SM10) immediately prior to FIB preparation and extraction. All submicron craters are scaled to share the scale bar in the image of SM5. M1 and M2 were located on Stardust foil C2113N-B, M3 and M4 were located on Stardust foil C2118N-B, and SM5–SM10 were located on Stardust foil C2113N-A. The FIB extractions were placed horizontally and through the center of the craters.

Al peak. Six submicron craters (SM5–SM10) were selected for further study with FIB-TEM techniques based on the strength of the observed SEM-EDS signals (Table 1; Fig. 2).

Cross sections of the micron-scale craters were prepared for TEM analyses by in situ FIB lift-out with Washington University's FEI Quanta 3D FIB with an attached Omniprobe micromanipulator. The FIB crater

Table 1. Characteristics of the craters selected for further FIB-TEM analysis. Crater diameters are measured from the midpoints of each crater rim. Crater depths are measured from the top of the crater to the deepest location of the protective Pt cap deposited during the FIB extraction process. Observed elements are listed in order of decreasing peak intensity.

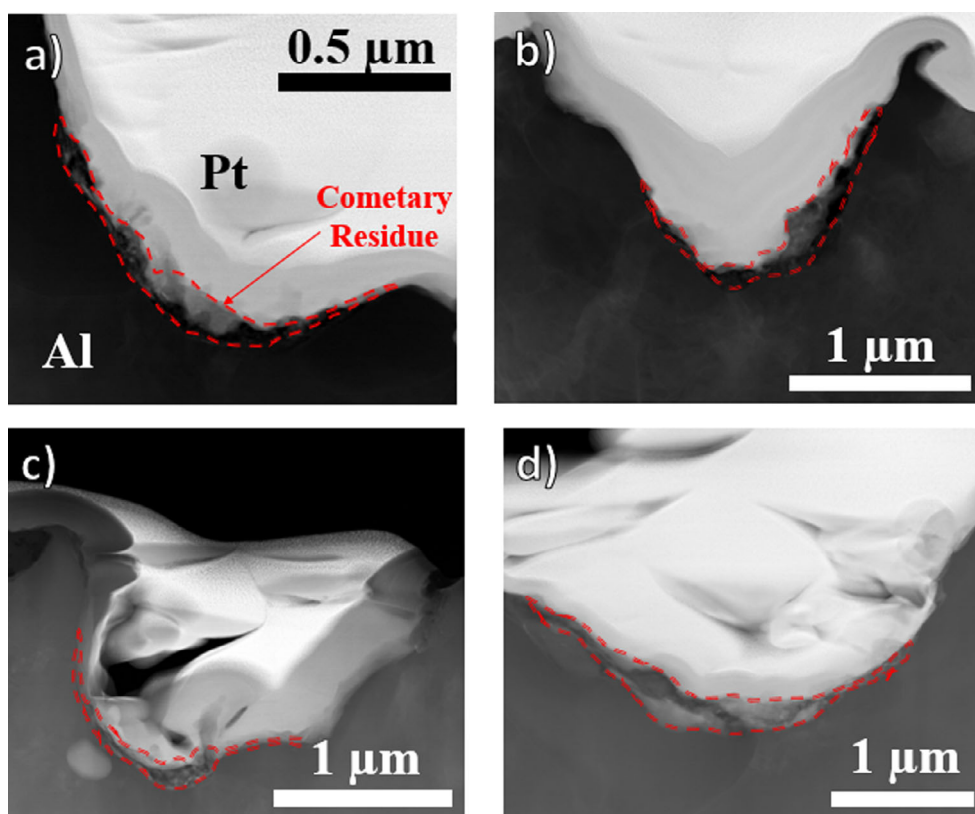| Crater type	Crater	Crater diameter (µm)	Crater depth (µm)	Depth/diameter ratio	Elements observed (SEM-EDS)
Micron-scale	M1	1.81	1.16	0.64	Si, Mg, Fe, S
	M2	3.12	1.42	0.46	Mg, Si, Fe, S
	M3	1.85	1.29	0.70	Si, Mg, Fe, S
	M4	5.20	2.20	0.42	Mg, Fe, Si, S, Ca
Submicron	SM5	0.34	0.16	0.47	Fe, S, Si, Ca
	SM6	0.24	0.14	0.58	Si, Fe, S
	SM7	0.33	0.16	0.48	Fe, S, Ca, Si
	SM8	0.22	0.06	0.27	Si
	SM9	0.23	0.11	0.48	Fe, S, Si
	SM10	0.38	0.18	0.47	Fe, S

Fig. 2. STEM HAADF images of cometary residue (highlighted in red) in micron-scale craters (a) M1, (b) M2, (c) M3, and (d) M4. The protective Pt coat deposited during FIB sample preparation appears brighter than the aluminum foil substrate, with the electron beam-deposited Pt appearing slightly darker than the Ga beam deposited Pt. Crater M3 has a Fe-rich impurity present beneath its residue layer that appears brighter than the surrounding Al. (Color figure can be viewed at wileyonlinelibrary.com.)

extraction procedure followed the steps outlined in Leroux et al. (2008a). The craters were protected with a Pt cap deposited with the electron beam at 5 kV to minimize damage to the crater residue layers from exposure to the Ga^+ ion beam. The Pt deposition was sufficiently thick to fill the entire crater interior as well as extend several hundred nanometers above the crater lips. The crater cross sections were extracted and welded to the exterior edges of Cu Omniprobe TEM support grids using Pt deposition. Further milling thinned the crater cross sections to 100–150 nm in order to allow for sufficient electron transparency to perform TEM-EDS analyses while also maximizing the preservation of cometary material for potential additional studies (e.g., secondary ion mass spectroscopy). The micron-scale craters underwent a final polish performed at the Naval

Research Laboratory (NRL) with a FEI Helios FIB operated at 8 kV. Cross sections of the submicron craters were fully prepared using Washington University's FEI Quanta 3D FIB using the same techniques that were applied to the micron-scale craters.

We performed bright-field imaging, high-angle annular dark-field imaging, and STEM-EDS characterization of the micron-scale crater residues with NRL's Nion UltraSTEM 200X aberration-corrected scanning transmission electron microscope (STEM) equipped with a Buker Xflash 100 windowless SDD-EDS operated at 200 kV. Quantification of the EDS spectra was performed with Cliff-Lorimer techniques using precalculated K-factors. Bright-field and dark-field imaging and SAED analyses of the submicron crater residues were performed with Washington University's JEOL 2000FX TEM operated at 200 kV. TEM-EDS characterization was performed on the same instrument operated at 160 kV utilizing a ThermoNoran System Six EDS system. We performed TEM-EDS analyses at 160 kV rather than 200 kV in order to improve the electron interaction cross section and improve overall X-ray count rates while also maintaining sample transparency for imaging. Our analysis spot diameters ranged from 50 to 75 nm. Quantification of the EDS spectra was performed with NIST DTSA-II software (Ritchie 2011, 2012) using elemental standards to perform Cliff-Lorimer analysis coupled with ZAF corrections primarily applied to light elements. Sample thicknesses were estimated to be ~125 nm for quantification. Further imaging and elemental mapping was performed on Washington University's JEOL JEM-2100F Field-Emission STEM operated at 200 kV with an attached Bruker SDD EDS system. All crater analyses calculated O abundances from the O-K peak areas, rather than inferred from oxide abundances. Counts from Al, Pt, and Cu were included in the spectral fitting and deconvolution, but were excluded from the analytical totals because they arise primarily from the Al foil substrate, the protective Pt coat applied during the FIB process, and the Cu TEM grid, respectively.

RESULTS

Foils C2113N-B and C2118N-B Micron-Scale Craters (M1–M4)

Secondary electron images (Fig. 1) of the micron-scale craters (M1–M4) reveal that they had complex crater floor shapes and retained residue distributions indicative of fine-grained, multicomponent aggregate impactors. This was confirmed in the TEM images (Figs. 3 and 4) and EDS maps (Figs. 5–16) of the crater cross sections. All of the crater shapes were consistent
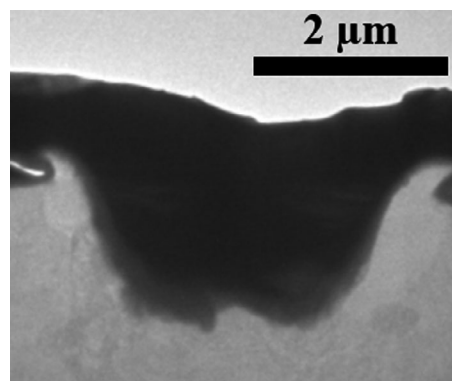

Fig. 3. TEM bright-field image of crater M1 showing its double-bowl structure.

with nominally normal incidence impactors. Crater M4's center was significantly deeper than the surrounding interior of the crater (Fig. 1), potentially indicating that the center of its impactor was denser than the material surrounding it.

Elemental compositions of the residues were obtained from selected regions of the raw count full spectrum images. The concentrations of Al, Pt, and Cu have been excluded from quantification due to the majority of their signals originating from the foil substrate, FIB preparation, and TEM grid, respectively. Minor Ti signal can also result from the Nion STEM sample holder. Crater compositions, excluding Al, Pt, and Cu, are constrained to sum to 100 atom%.

Micron-Scale Crater 1 (M1)

The crater residue is separated into two bowl-shaped indentations located on each side of the crater, indicative of a bilobate impactor (Fig. 3). Residue is concentrated on the floors of the indentations with little residue connecting them. Residue thickness reaches 150 nm in the bowls and slowly tapers off along the crater walls.

The residue is largely composed of combinations of Mg- and Si-rich materials and iron nickel sulfides (Fig. 4; Table 2). Si and Mg are generally well correlated in the residue, with Si/Mg ratios ranging from 1.05 to 1.85. Large S abundances were only seen alongside large Fe abundances, indicating that the observed S was the result of iron sulfide impactors. However, Fe is abundant even in low-S regions, indicating that some of the Fe was likely contributed by Mg- and Si-rich impactor material. Fe/S ratios in the craters range from 2.0 in regions dominated by Fe and S to 5.7 in regions dominated by Mg- and Si-rich residues. Small (<1 atom%) amounts of Ti are present in some regions of the residue, typically alongside traces of Ca. One subregion of the residue contains a Ca hot spot; however, this subregion is not associated with
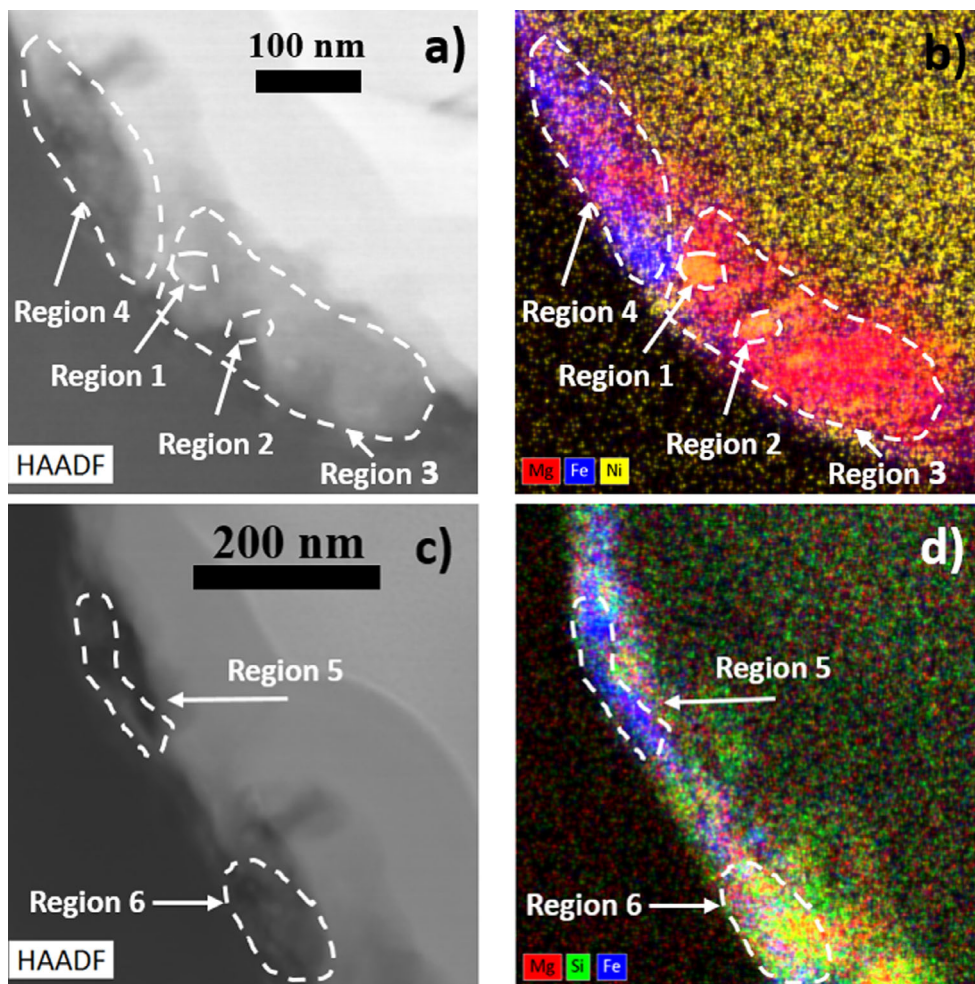
Fig. 4. a) STEM HAADF image of residue on the floor of crater M1 and (b) STEM EDS Mg-Fe-Ni map with analyzed regions (detailed in Table 2) highlighted. c) STEM HAADF image of another subsection of crater M1 and (d) STEM EDS Mg-Si-Fe map of residue from this subsection with analyzed regions (detailed in Table 2) highlighted. (Color figure can be viewed at wileyonlinelibrary.com.)

Ti. Trace (<0.5 atom%) Cr and K are dispersed throughout the crater residue.

Ni is present in the crater residue, but Ni abundances are not well correlated with S abundances (Fig. 4; Table 2). While low amounts of Ni are present throughout the crater, Ni largely appears as discrete ~10 nm spots. However, these subregions are located within Mg- and Si-rich melt regions. These Ni-rich spots also have slightly higher Fe abundances than the surrounding melt, suggesting that the impactor contained taenite subgrains surrounded by more Mg- and Si-rich materials.

Micron-Scale Crater 2 (M2)

The crater residue is largely spread across the floor and the right wall of the crater (Fig. 3). Residue thickness reaches 200 nm along the crater wall.

The residue is largely composed of combinations of Mg- and Si-rich materials and iron sulfides (Fig. 5; Table 2). Si and Mg, though located throughout the crater residue, are not well correlated in the thickest part of the residue along the right crater wall (Fig. 5). As a result, Mg/Si ratios range from 0.53 to 2.94 in the crater residues. Two regions (regions 2 and 5 in Fig. 5) have Mg/Si ratios and O abundances too large to be stoichiometrically consistent with pyroxene or olivine impactors. The large Mg and O abundances in these regions are potentially the result of spinel ($MgAl_2O_4$) impactors. We did not perform Al quantification of the crater residues due to the presence of Al signals throughout the residue resulting from intermixing with the Al foil substrate. Previous analog studies have observed Al from the foil combining with impacting material to form amorphous, glassy residue layers (Wozniakiewicz et al.
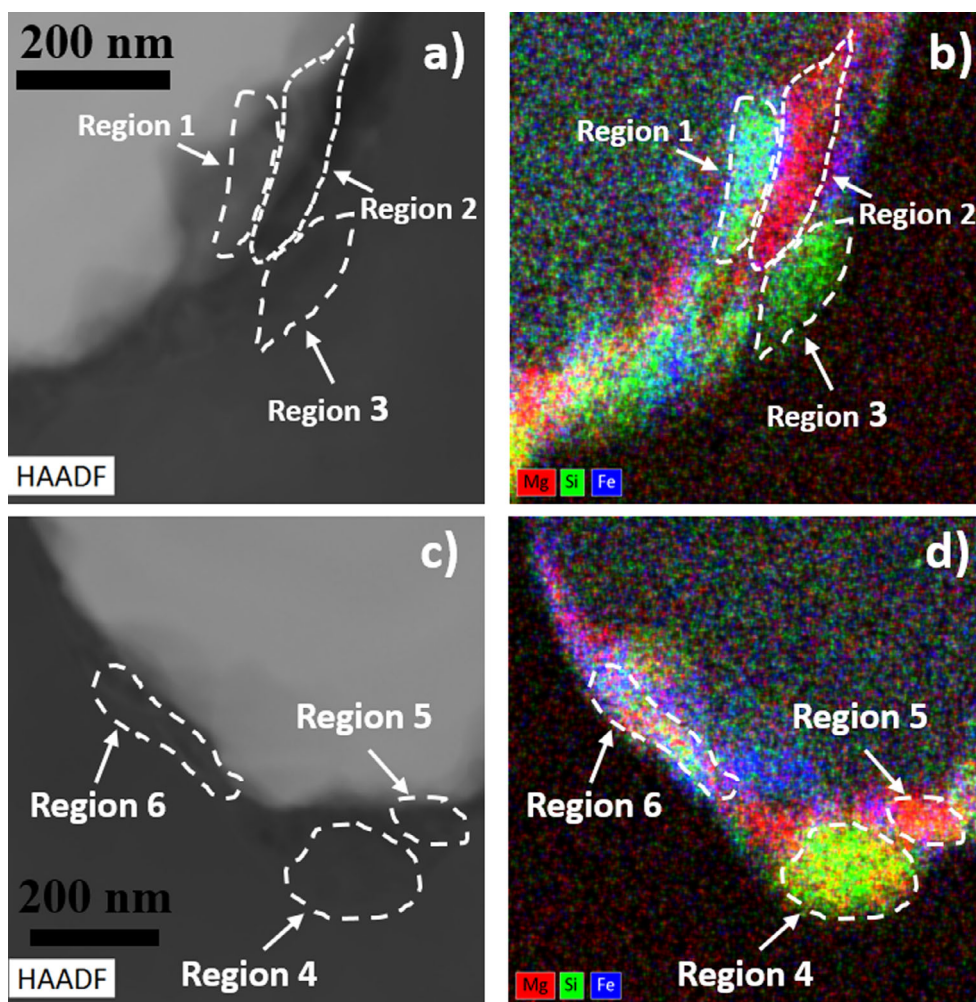
Fig. 5. a) STEM HAADF image of residue on the floor of crater M2 and (b) STEM EDS Mg-Si-Fe map with analyzed regions (detailed in Table 2) highlighted. c) STEM HAADF image of another subsection of crater M2 and (d) STEM EDS Mg-Si-Fe map of residue from this subsection with analyzed regions (detailed in Table 2) highlighted. (Color figure can be viewed at wile yonlinelibrary.com.)

2012b). However, assuming some of the observed Al from these regions were contributed by the impacting material would allow for a portion of these melt regions to be stoichiometrically consistent with a spinel impactor.

Fe and S abundances are generally well correlated in the crater residues, with Fe/S ratios ranging from 1.3 to 2.9 (Table 2). Some Fe was likely contributed by impacting Mg- and Si-rich materials (particularly in region 6 in Fig. 5) resulting in Fe/S ratios that are larger than those present in any impacting iron sulfide materials. Ni was only present in some of the iron sulfide residues with Fe/Ni ratios in these materials ranging from 6.3 to 16.9. Small (<1 atom%) amounts of Ti and trace (<0.5 atom%) Ca are also present throughout the crater residues.

Micron-Scale Crater 3 (M3)

The crater residue is largely concentrated in a single bulb located in the center of the crater's floor, with residue layers tapering away on either side of the bulb. Residue thickness ranges from 125 nm in the center of the bulb to 10 nm at the ends of the tapering residue layers.

Si and Mg are well correlated in the crater residue, with both elements composing similar fractions of the crater residues (Fig. 6; Table 2). Cr and Mn are present in the Si-rich regions of the residue in small amounts (<1 atom%) indicating that low iron, Mn-enriched (LIME) olivine or low iron, Cr-enriched (LICE) olivine may have contributed some of the observed silicate material (Zolensky et al. 2006; Komatsu et al. 2015).
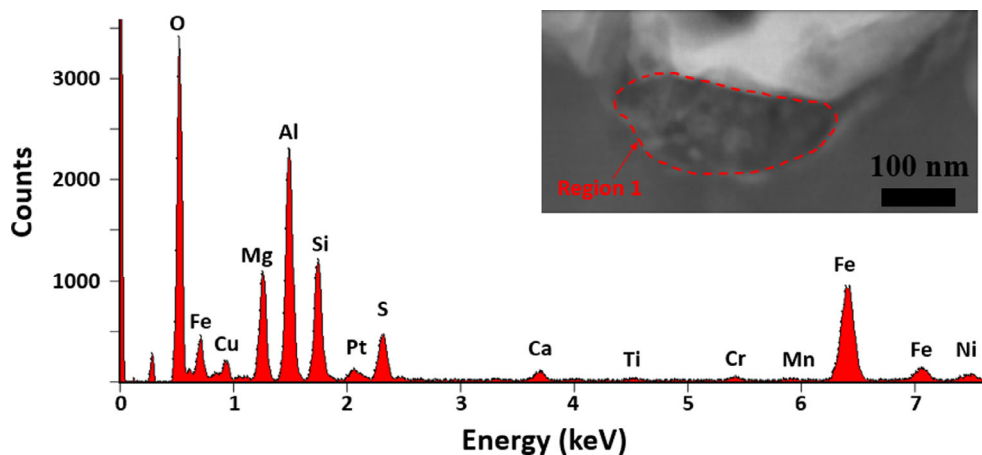
Fig. 6. STEM-EDS spectrum from the bulb of residue (region 1, pictured) from crater M3. The Al, Cu, and Ti peaks are likely the result of the Al foil substrate, the Cu TEM grid, and the Nion STEM sample holder, respectively. (Color figure can be viewed at wileyonlinelibrary.com.)
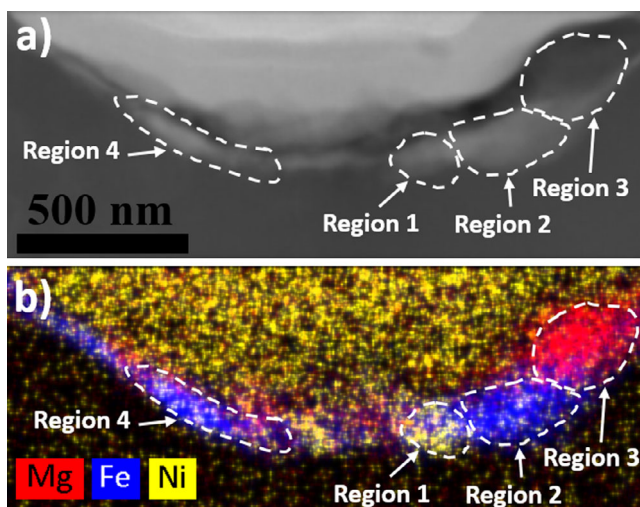

Fig. 7. a) STEM HAADF image of residue on the floor of crater M4 and (b) STEM EDS Mg-Fe-Ni map with analyzed regions (detailed in Table 2) highlighted. (Color figure can be viewed at wileyonlinelibrary.com.)

Fe, S, and Ni are well-correlated in the crater residues. Fe/S ratios are large and range from 3.7 to 7.5 while Fe/Ni ratios range from 5.5 to 10.8. The relatively large Fe/S ratios indicate that either S loss is widespread or that significant Fe was contributed from nonsulfide sources. The strong correlation between Fe and S in the crater residues, coupled with the likely presence of LIME or LICE olivine, suggests that S loss or other Fe sources (e.g., magnetite) are more likely to be the cause of the large Fe/S ratios. Ca is also present throughout the crater residue (<1 atom%) as well as trace (<0.5 atom%) K and Ti.

Micron-Scale Crater 4 (M4)

The crater residue is well distributed, covering most of the crater floor. Residue thicknesses range from 165 nm near the crater's center to 10 nm on the crater walls.

The residue is fully composed of combinations of Si-rich materials and iron nickel sulfides. Si and Mg are generally well correlated in the residue. The left side of the residue (Fig. 7, region 4) contains less Mg and more Fe than other Si-rich regions of the crater. Fe/S ratios within this region are the largest in the crater (3.3), suggesting that a portion of the Fe in this region may have originated from a silicate impactor. Fe and S are well correlated in the residue, but Ni, though only present in regions with high Fe and S abundances, appears in discrete subregions of the iron sulfides (Fig. 7, region 1). As a result, while Fe/S ratios in the crater only range from 1.6 to 3.3, Ni/S ratios range from 6.2 to 59.4. The Ni-rich subregions are associated with both large Fe and S abundances, indicating that these regions may be the result of small Ni-rich iron nickel sulfides (e.g., pentlandite) composing a fraction of the impacting sulfide materials. Trace (<0.5 atom%) Ca and Ti are also present in the crater residue.

Foil C2113N-A Submicron Craters (SM5–SM10)

Submicron craters SM6–SM10 have rounded, bowl-shaped crater bottoms indicative of a compact impactor. Crater SM5 contains a double-bowl shape, suggesting the impactor was bilobate with a central region of lower mass or lower density (Fig. 8). Crater SM8, though containing a bowl-shaped bottom, has no
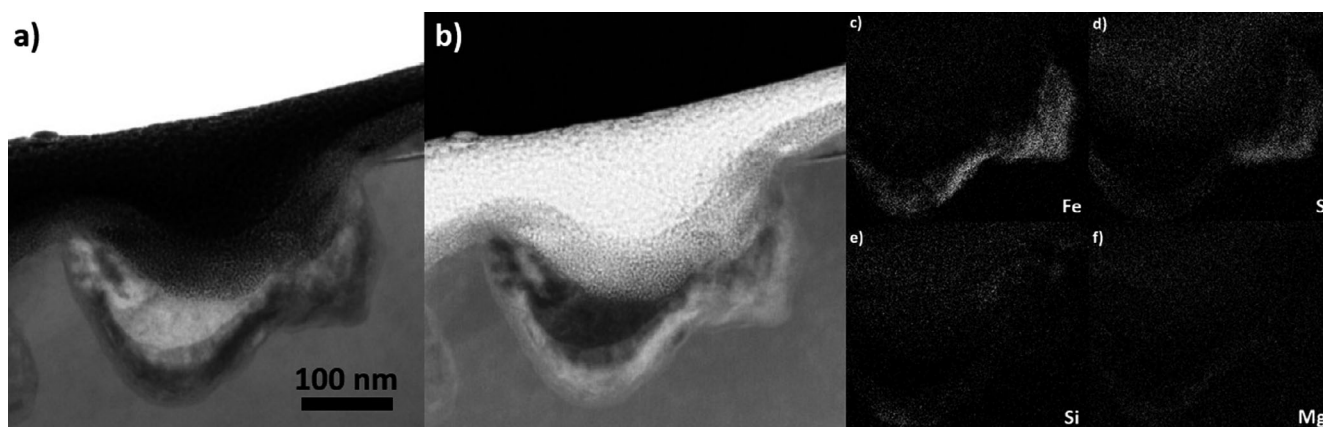
Fig. 8. a) Bright-field and (b) high-angle annular dark field STEM images taken of crater SM5 at 300k magnification. STEM-EDS K-line maps of (c) Fe, (d) S, (e) Si, and (f) Mg.
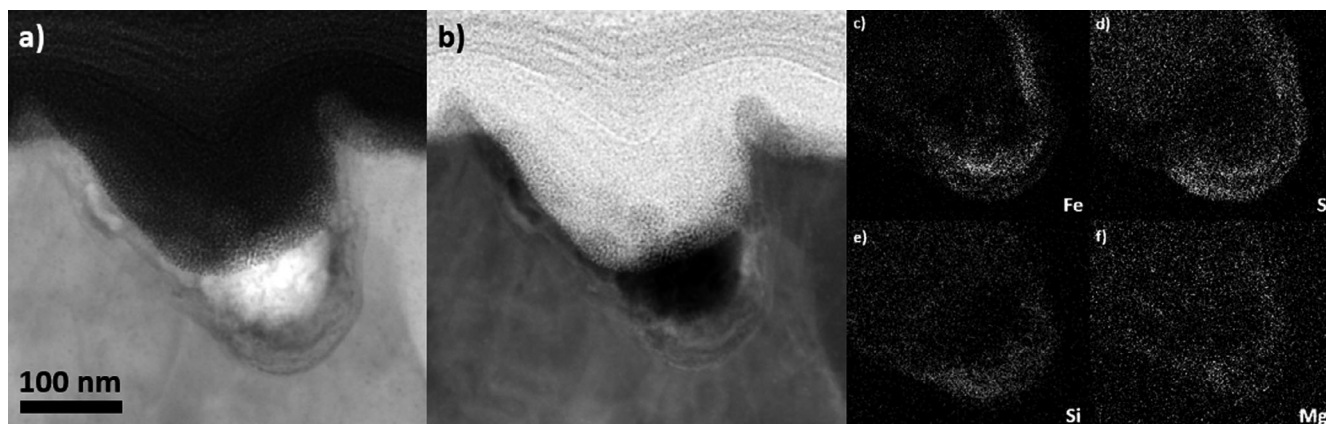

Fig. 9. a) Bright-field and (b) high-angle annular dark field STEM images taken of crater SM6 at 600k magnification. STEM-EDS K-line maps of (c) Fe, (d) S, (e) Si, and (f) Mg.

discernable residue layer. All the craters have fairly symmetric shapes that are generally consistent with acute angles of incidence relative to the surface normal for the impacting material (Kearsley et al. 2007).

No crystalline material was observed in the crater residues. Materials in the residue layers are largely heterogeneous, indicative of rapid melting and resolidification (Wozniakiewicz et al. 2012b). Elemental characterization of the submicron craters is detailed in Fig. 15 and Table 3.

Submicron Crater 5 (SM5)

The crater residue is separated into two bowl-shaped indentations located on each side of the crater that are connected by a thinner melt layer (Fig. 8). Residue thickness is 40 nm along the tops of the crater walls, 95 nm in the smaller of the indentations, and 180 nm in the larger indentation.

Si and Mg are a minor part of the residue with the majority of the residue composed of less than 2.5 atom% for each element (Table 3). Oxygen is abundant throughout the residue. The large O to Si ratios are not stoichiometrically consistent with olivines or pyroxenes which have been observed frequently in Stardust collection media (Zolensky et al. 2006). The right side of the crater is dominated by the presence of iron-nickel sulfide residues. Fe/S ratios in this region of the crater range from 1.4 to 2.0 while Fe/Ni ratios range from 12.2 to 26.9. The region separating the two crater depressions contains high Fe though this was not correlated with an increase of S or Ni, suggesting an alternate Fe source than iron nickel sulfides. Ca is present in small amounts throughout the crater residue (1–3 atom%), along with trace K (<1 atom%). Zn is the most abundant element on the left side of the crater, composing up to 63.0 atom% of regions on the left crater walls. Zn abundance is not correlated with S
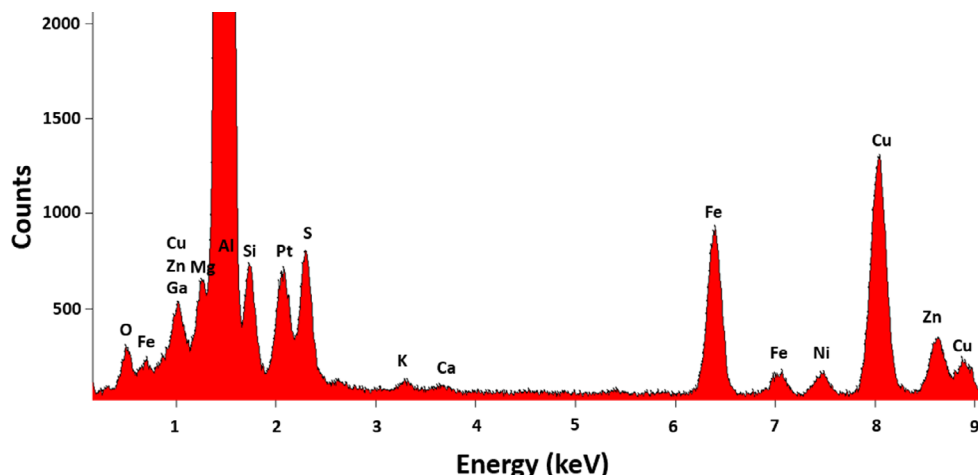
Fig. 10. TEM-EDS spectrum of the full residue layer of crater SM6. The Al, Pt, Ga, and Cu peaks are likely the result of the Al foil substrate, the protective Pt coat applied during the FIB process, Ga embedded from the FIB's Ga+ ion beam, and the Cu TEM grid, respectively. (Color figure can be viewed at wileyonlinelibrary.com.)
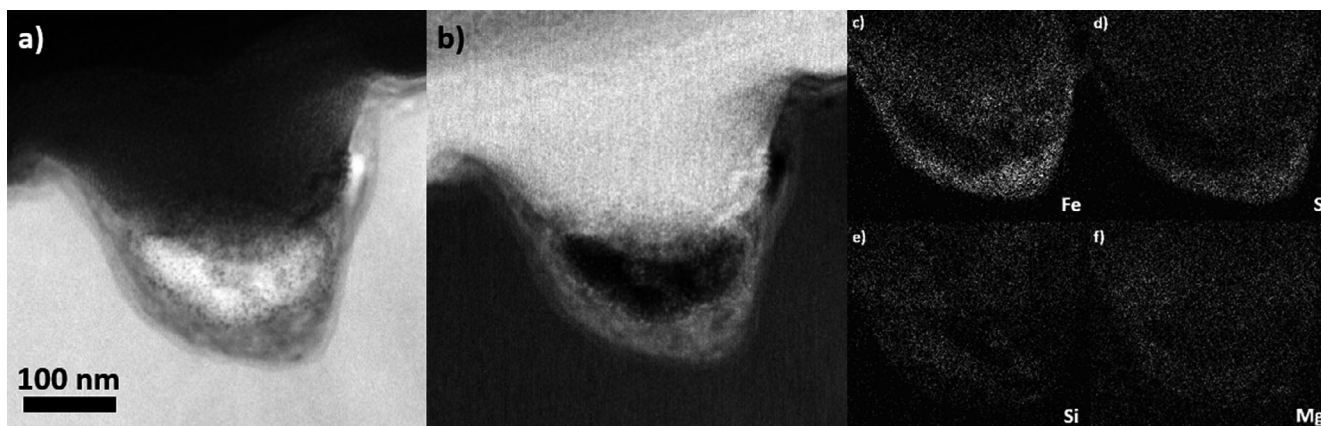

Fig. 11. a) Bright-field and (b) high-angle annular dark field STEM images taken of crater SM7 at 400k magnification. STEM-EDS K-line maps of (c) Fe, (d) S, (e) Si, and (f) Mg.
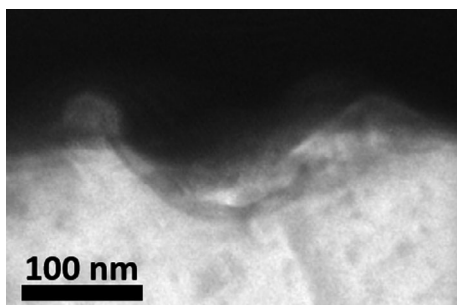
Fig. 12. Bright-field TEM image of crater SM8 at 200k magnification.

abundances, demonstrating that the Zn is unlikely to originate from sulfide impactors. The regions with the highest Zn concentrations also contain up to 5.0 atom% Mn. Zinc sulfides are the most likely source of the extremely high Zn abundances within the crater, but the lack of S within the Zn-rich residues suggests the excessive Zn is the result of contamination rather than captured cometary material.

Submicron Crater 6 (SM6)

Residue in the crater bottom is slightly skewed to one side with the thickest part of the residue lying off center. Residue thickness ranges from 20 nm on the crater walls to nearly 100 nm at the crater bottom (Fig. 9).

Si and Mg are present throughout the crater residue (Table 3). Si is nearly three times as abundant as Mg with residue in the crater bottom composed of 7.5 and

Fig. 13. a) Bright-field and (b) high-angle annular dark field STEM images taken of crater SM9 at 500k magnification. STEM-EDS K-line maps of (c) Fe, (d) S, (e) Si, and (f) Mg.
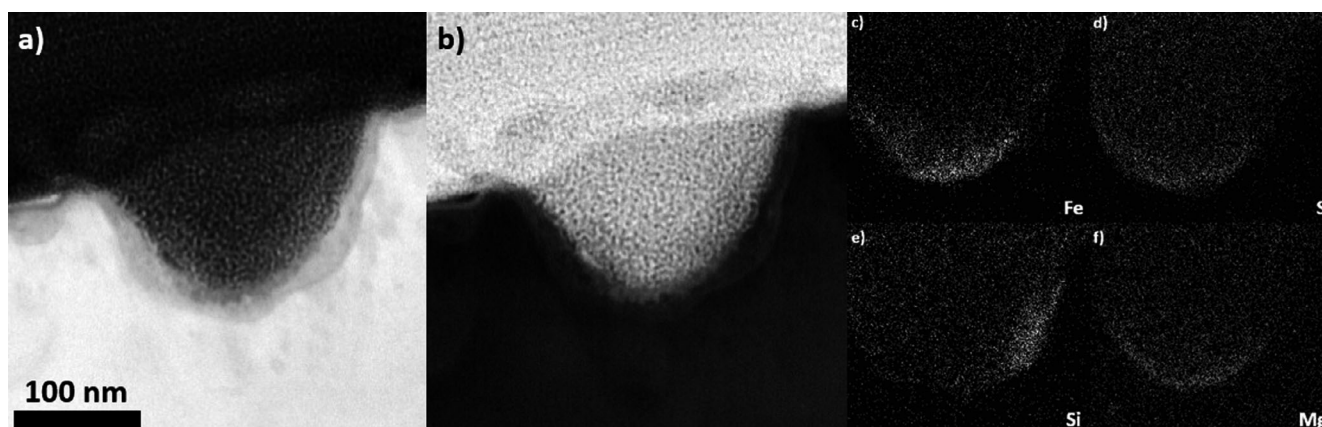
2.8 atom% of Si and Mg, respectively. O is abundant throughout the crater, resulting in O/Si ratios greater than 6.0 throughout the crater residue. Fe, S, and Zn are also major components of the crater residue (Fig. 10). The Fe/S ratio of material in the crater bottom is 1.36. The (Fe+Zn)/S ratio of this material is 2.52, suggesting that sulfur loss occurred if iron and zinc sulfides were the primary sources of these elements. Ni abundances are high relative to Fe abundances, with an Fe/Ni ratio of 5.54 for material in the crater bottom.

Submicron Crater 7 (SM7)

The crater residue is distributed symmetrically. Residue in the crater bottom is of a similar size to that seen in crater SM6, with thicknesses ranging from 20 nm on the crater walls to 100 nm at the center of the crater's bowl (Fig. 11).

The crater residue contains Si and Mg throughout with Si abundances ranging from 4.5 to 8.8 atom% and Mg abundances ranging from 3.2 to 4.5 atom% (Table 3). Si/O ratios consistently range between 4.0 and 5.0, placing Si abundances slightly too low for olivinic stoichiometry. Iron nickel sulfides are the dominant phase in the crater residues with Fe/S ratios and Fe/Ni ratios ranging from 0.89 to 1.28 and 15.9 to 24.3, respectively. Zn is present throughout the crater in smaller abundances (2.5–3.5 atom%), suggesting zinc sulfides are a component of the impacting material. Ca is also present throughout the crater residue (0.9–3.4 atom%).

Submicron Crater 8 (SM8)

This crater is extremely shallow, having a depth of only 60 nm and a depth to diameter ratio of 0.27

(Fig. 12). This depth to diameter ratio is smaller than ratios seen in previously investigated Stardust craters and analogs fired at ~6.1 km s^{-1} (Kearsley et al. 2007; Leroux et al. 2008a). No residue was observed in the crater bottom. The crater may have been an irregularity in the aluminum foil itself arising from the removal of Fe- and Ni-rich precipitates during foil manufacturing (Stroud et al. 2014) rather than the result of a cometary impactor, explaining the small depth to diameter ratio. However, this alone would not explain the weak Si signal seen during the SEM-EDS analysis as no Si was observable during TEM-EDS analysis. Another possibility is that we missed the center of the crater during the final cross section thinning of the FIB preparation procedure. In this case, we may have created a cross section lacking the deepest part of the crater as well as any impactor residue, which also allows for the lack of Si in TEM-EDS spectra if the crater was not cometary in origin. A third option is that the crater was the result of a secondary impactor, potentially from the Stardust solar cell glass, which is rich in Si and has been observed many times in the interstellar Stardust foil (Stroud et al. 2014). Such an impactor could have produced the Si signal seen during SEM-EDS analysis, as well as created an asymmetric, shallow crater whose residue was later missed during the FIB extraction due to an asymmetric residue layer. However, the lack of an obvious splash rim, as well as the well-rounded crater bottom, suggest that the crater is not the result of a secondary impact.

Submicron Crater 9 (SM9)

The impactor residue is thin and uniform around the crater, with the crater residue ranging from 15 to 30 nm deep (Fig. 13).
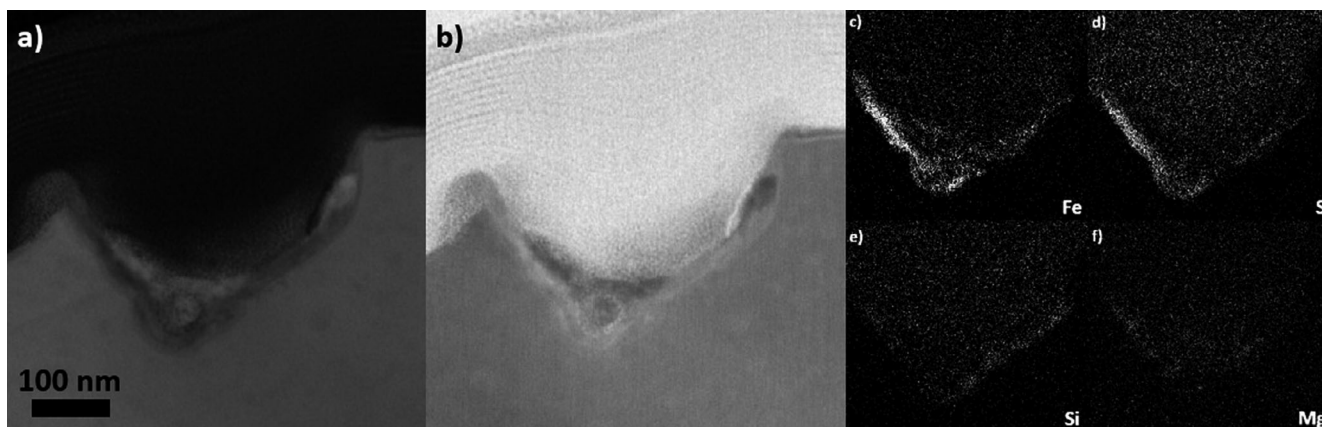
Fig. 14. a) Bright-field and (b) high-angle annular dark field STEM images taken of crater SM10 at 300k magnification. STEM-EDS K-line maps of (c) Fe, (d) S, (e) Si, and (f) Mg.
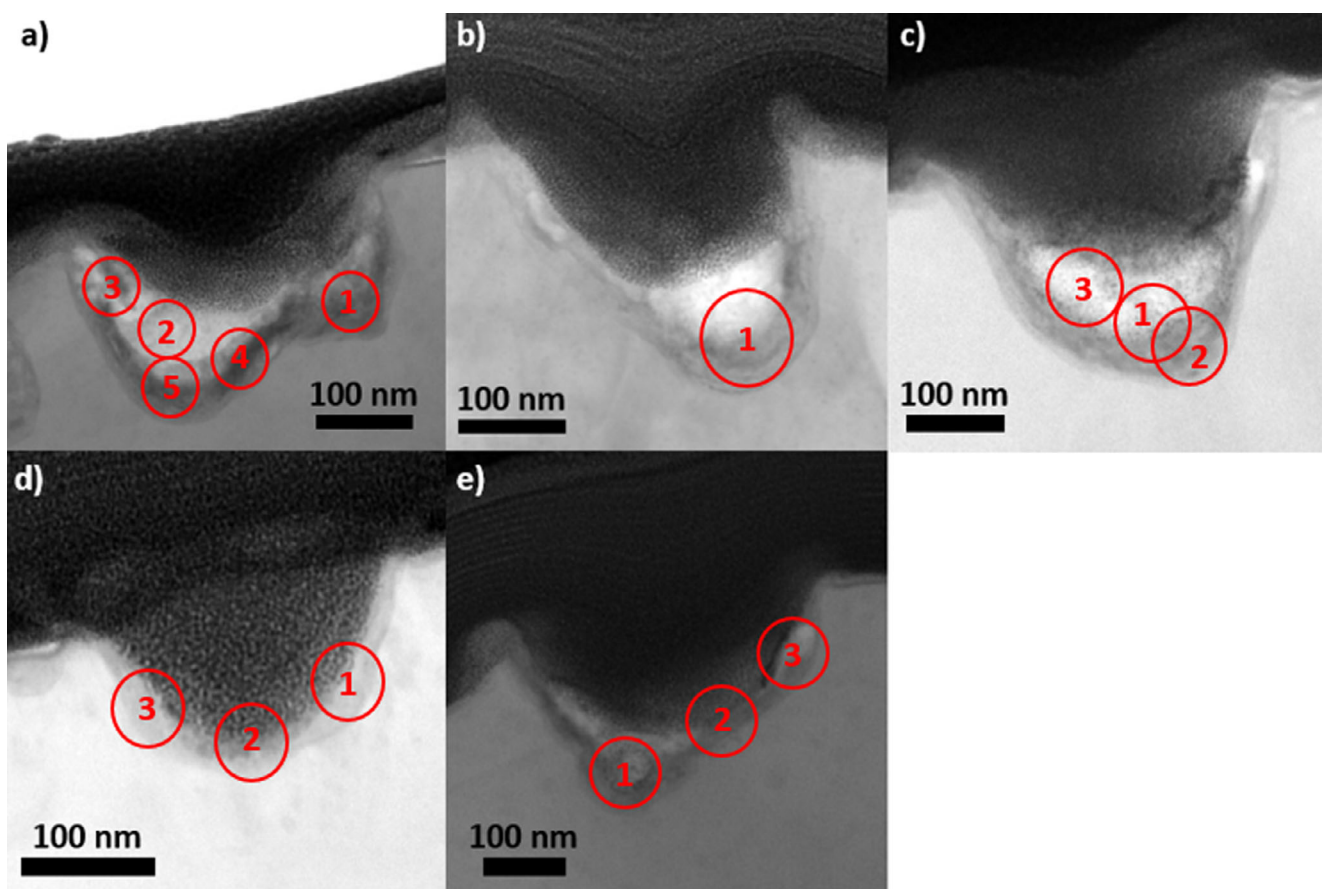
Fig. 15. TEM images of submicron craters (a) SM5, (b) SM6, (c) SM7, (d) SM9, and (e) SM10 with labeled regions that are reported in Table 3. (Color figure can be viewed at wileyonlinelibrary.com.)

The crater residue is highly heterogeneous. The right side of the crater contains abundant Si composing up to 28.5 atom% of the residue material (Table 3). Mg abundance is not correlated with Si, and despite high Si concentrations being present Mg was never observed above 4.0 atom%. O/Si values range from approximately 2.0–7.5 throughout the crater, potentially allowing for olivine or pyroxene as sources of the observed Si, though the crater's thoroughly heterogeneous composition and lack of crystalline material makes positive identification of these minerals difficult. The left side and center depression of the crater contained more Fe than Si, with
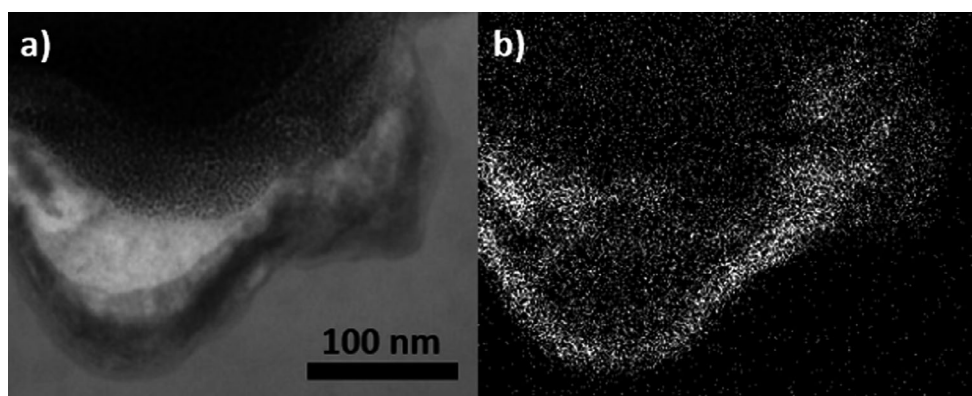
Fig. 16. a) Bright-field STEM image of crater SM5 and (b) STEM-EDS Zn map of the same region.

Table 2. Representative compositions (atom%) for craters M1–M4 for elements with calculated abundances $\geq$ 0.5 atom%. Elements that were detected with abundances $<$ 0.5 atom% are listed as trace (tr) elements. The crater totals were calculated using the EDS spectra collected for the entire crater residue, and thus are not averages of the values reported for individual regions. Other elements not present in the table that were also observed are listed in the other column. All elements listed in the other column only had trace ($<$ 0.5 atom%) detections.

| Crater	Region	O	Mg	Si	Fe	S	Ni	Ca	Ti	Other
M1	1	62.5	11.1	11.7	7.3	2.3	5.1	nd	nd	na
	2	67.5	7.9	14.6	5.7	1.0	3.2	nd	nd	na
	3	68.5	10.6	12.8	4.8	1.1	0.7	tr	tr	na
	4	59.8	8.4	9.7	13.3	6.6	0.7	1.0	0.5	Cr, K
	5	59.8	9.3	10.1	13.3	5.9	0.5	1.1	nd	na
	6	46.9	5.3	6.7	27.2	13.1	0.8	nd	nd	na
	Total	60.7	8.4	12.4	10.9	5.6	0.7	0.7	0.6	Cr, K
M2	1	68.7	5.5	10.4	8.1	6.4	nd	nd	0.9	na
	2	78.6	9.4	3.2	4.4	3.4	nd	tr	0.5	na
	3	88.2	nd	8.0	2.0	1.8	nd	nd	nd	Na
	4	58.1	14.5	23.0	2.8	1.6	nd	nd	nd	na
	5	65.3	16.9	7.5	5.7	3.7	0.9	nd	nd	na
	6	60.9	9.2	10.1	13.5	4.7	0.8	nd	0.8	na
	Total	73.1	8.0	7.3	6.5	4.1	0.2	tr	0.6	na
M3	1	59.0	7.7	9.1	16.3	3.9	1.5	0.8	tr	Mn, Cr, K
	Total	57.5	7.5	8.0	17.9	4.3	2.5	0.8	nd	Mn, Cr, K
M4	1	23.9	nd	nd	41.1	28.5	6.6	nd	nd	na
	2	26.5	3.2	2.9	41.6	25.0	0.7	nd	nd	na
	3	61.1	11.1	12.2	11.4	4.2	nd	nd	nd	na
	4	45.4	5.5	8.9	30.8	9.3	nd	nd	nd	na
	Total	45.3	6.0	7.2	26.4	13.0	1.3	tr	tr	na

nd, element was not detected; na, value is not available.

Fe compositions ranging from 13.2 to 20.1 atom%. Fe abundance is correlated with S and Ni, and Fe/S ratios range from 0.67 to 1.0 on the left side of the crater. Zn is also present in the Fe-rich regions of the crater, with measured abundances ranging from 0.6 to 2.6 atom%.

Submicron Crater 10 (SM10)

Residue within the crater is heavily concentrated into one bulb located slightly off-center from the crater's deepest point (Fig. 14). The residue thickness ranges from 15 nm along the crater walls to 90 nm in the off-center bulb.

Si is present throughout the crater residue, with Si abundances ranging from 6.0 to 10.3 atom% (Table 3). Mg is largely absent and generally not detected, though Mg abundances in some regions reached 2.0 atom%. Si and O abundances were correlated, though O/Si ratios are typically close to 7.0 and far above stoichiometries consistent with olivine or

B. A. Haas et al.

Table 3. Representative compositions (atom%) for submicron crater residue regions measured by TEM-EDS. The crater residue regions are shown in Figure 15. Uncertainties are listed in parentheses, rounded up to the nearest 0.1%. Al, Pt, and Cu have been excluded from quantification due to possible contamination from the foil substrate, FIB preparation, and TEM sample holder, respectively.

Crater	Subregion	O	Si	Mg	Fe	S	Ni	Ca	Zn	Other elements	O/Si	Fe/S	Fe/Ni
SM5	1	21.5 (1.0)	2.2 (0.1)	nd	36.1 (0.4)	25.8 (0.3)	1.3 (0.1)	1.1 (0.1)	11.5 (0.1)	K	9.77	1.40	26.9
	2	39.4 (0.2)	1.7 (0.1)	nd	7.4 (0.1)	4.2 (0.1)	0.6 (0.1)	2.3 (0.1)	37.9 (0.6)	K, Mn	23.2	1.75	12.2
	3	26.7 (0.6)	0.9 (0.1)	1.3 (0.1)	3.2 (0.1)	1.3 (0.1)	0.2 (0.1)	2.9 (0.1)	63.0 (0.3)	K, Mn, Cl	29.7	2.48	16.6
	4	45.4 (0.5)	1.7 (0.1)	0.7 (0.1)	22.3 (0.2)	3.4 (0.1)	0.7 (0.1)	1.9 (0.1)	22.3 (0.1)	K	26.7	5.72	33.2
	5	43.0 (0.5)	6.6 (0.1)	1.0 (0.1)	15.9 (0.1)	4.5 (0.1)	0.9 (0.1)	2.1 (0.1)	25.7 (0.1)	K	6.51	3.50	17.6
SM6	1	46.6 (0.5)	7.5 (0.1)	2.8 (0.1)	15.3 (0.3)	11.2 (0.1)	2.8 (0.1)	0.2 (0.1)	13.0 (0.1)	K	6.21	1.36	5.54
SM7	1	35.3 (1.0)	8.1 (0.1)	3.7 (0.1)	25.4 (0.5)	19.8 (0.3)	1.6 (0.1)	2.6 (0.1)	3.5 (0.2)	nd	4.36	1.28	15.9
	2	22.8 (1.3)	4.9 (0.1)	3.2 (0.1)	31.4 (0.4)	35.1 (0.4)	1.5 (0.1)	0.9 (0.1)	nd	Ti	4.65	0.89	21.5
	3	42.6 (0.8)	8.8 (0.1)	4.3 (0.1)	21.1 (0.4)	16.5 (0.3)	0.9 (0.1)	3.4 (0.1)	2.5 (0.2)	nd	4.85	1.28	24.3
SM9	1	60.5 (0.4)	28.5 (0.9)	0.4 (0.2)	7.3 (0.1)	2.4 (0.2)	1.0 (0.2)	nd	nd	nd	2.12	3.05	7.25
	2	35.9 (1.3)	5.6 (0.1)	4.0 (0.1)	20.1 (0.5)	31.3 (0.9)	1.6 (0.1)	0.1 (0.1)	0.6 (0.4)	nd	6.42	0.67	12.9
	3	53.1 (0.4)	7.5 (0.1)	2.4 (0.1)	13.2 (0.4)	19.7 (0.6)	1.6 (0.2)	nd	2.6 (0.4)	nd	7.08	0.67	8.52
SM10	1	41.5 (1.0)	6.0 (0.1)	nd	20.6 (0.5)	26.9 (0.7)	1.4 (0.2)	1.3 (0.1)	3.4 (0.3)	nd	6.92	0.77	14.4
	2	58.2 (0.1)	7.9 (0.1)	1.9 (0.1)	11.1 (0.2)	8.8 (0.1)	0.9 (0.1)	0.2 (0.1)	10.7 (0.1)	Ti	7.37	1.26	13.1
	3	73.3 (1.8)	10.3 (0.5)	nd	7.4 (0.3)	1.2 (0.3)	nd	0.6 (0.1)	4.7 (0.4)	Ti, K, Cl	7.11	6.72	na

nd, element was not detected; na, value is not available. Crater SM8 is not listed as it did not contain residue.

pyroxene. O and Si abundances are anti-correlated with Fe, S, and Ni abundances. Fe, S, and Ni compose up to half the residue material in the upper right portion of the residue, with Fe/S and Fe/Ni ratios ranging from 0.77 to 1.26 and 13.1 to 14.4 in this region, respectively. Zn is also common in the crater residue with abundances typically close to 4.0 atom% but ranging as high as 10.7 atom%. Small amounts (<1.5 atom%) of Ca and Ti are also observed in the crater residues.

DISCUSSION

Submicron Impactor Distribution

Our search for submicron craters in this study required us to thoroughly examine a 5.28 mm^2 section of foil C2113N-A. As a result, we are capable of comparing our crater spatial density with previous searches of Stardust foils. We observed 20 crater-like features across the section of foil C2113N-A that we searched; however, only 10 craters returned SEM-EDS results indicating the presence of potential cometary material. Only counting craters with positive SEM-EDS results, we observed 1.89×10^6 impacts per m^2 on our section of foil C2113N-A. These results are largely consistent with previous Stardust foil studies, which for projectile diameters ranging from ~125 to ~250 nm and assumed impactor densities of 2.4 g cm^{-3} observed between ~1×10^6 and ~5×10^6 cumulative impactors per m^2 (Hörz et al. 2006; Kearsley et al. 2006). However, our crater spatial density was still significantly lower than some other previously studied Stardust foils, such as foil C2052N, which had 166 observed craters and an areal density of ~2×10^7 cumulative impactors per m^2 across crater impactors similar to our own in size (Hörz et al. 2006).

Crater Morphology

The morphologies of the craters, aside from crater SM8, which contains no observable residue, are largely consistent with previous investigations of analog and authentic Stardust impactors. The craters' rounded, bowl-shaped bottoms differ from the shallow, elongated crater shapes indicative of terrestrial contamination in the form of secondary impacts from material native to the Stardust spacecraft (Stroud et al. 2014). Depth/diameter ratios of the micron-scale craters (M1–M4) range from 0.42 to 0.70, with an average value of 0.56. Depth/ diameter ratios of residue-containing submicron craters (M5–M7, M9, and M10) range from 0.47 to 0.58, with an average value of 0.50. Investigations of silicate mineral impactors on flight-spare Stardust foils fired at

6.1 km s^{-1} found depth/diameter ratios largely centered between 0.52 and 0.65 with our values (between 0.42 and 0.70) still lying within the first three SDs (Kearsley et al. 2008). Our depth/diameter ratios in the submicron craters may have been slightly smaller than average due to our impactors having lower densities or higher porosities than the previously investigated silicate impactors, as both factors can result in smaller depth/diameter ratios (Kearsley et al. 2007). However, depth/diameter ratios can be affected by a number of other factors, such as angle of incidence, impactor velocity, and volatile contents, making the determination of impactor density or porosity difficult (Price et al. 2010).

Lack of Crystalline Material

The micron-scale craters (M1–M4) were only investigated with STEM techniques, and thus, the crystallinity of the material was not observed. However, none of our investigated submicron craters (SM5–SM10) contain any crystalline material. These results are unexpected given that previous reports on FIB-TEM investigated Stardust craters returned crystalline material in 10 of 22 investigated craters (Leroux et al. 2008a, 2010; Stroud et al. 2010). Additionally, previous investigations have suggested that smaller crystalline impactors are less likely to be amorphized during impact processing (Croat et al. 2015) and our investigation focused on craters smaller than the majority of those previously reported to contain surviving crystalline material. Studies focused on coarser grains captured by the Stardust aerogels have also indicated that crystalline materials are abundant in Wild 2 (Zolensky et al. 2006).

Analog studies have shown that crystalline material is frequently destroyed during impact processing on the foils, particularly when the impactor is an aggregate of crystalline subgrains (Wozniakiewicz et al. 2012b). Given that our craters are universally aggregates of silicate and iron sulfide components, the possibility exists that all impacting crystalline material was destroyed during the collection process. An alternative explanation for our lack of crystalline material is that our impactors were amorphous prior to impact. Astronomical observations have shown comets contain abundant amorphous silicates (Hanner 2003). Studies of fine-grained Wild 2 components collected by the aerogel tiles have found amorphous silicates and iron sulfide vesicles constituting GEMS-like material to be abundant (Stodolna et al. 2012), though that GEMS-like material may have resulted from melting and intermixing of the Stardust aerogel with crystalline materials that contained silicates and sulfides (Ishii et al. 2008; Ishii 2019). The metal and sulfide nanograins inside GEMS are

crystalline, but there is a strong possibility that our impactor residues are a quenched combination of amorphous silicates and formerly crystalline sulfides (Keller and Messenger 2011). However, it is difficult to prove any impactor material was amorphous prior to collection given the impact conditions.

Silicate and Iron Sulfide Abundances

Silicon was observed throughout the studied craters. Excluding crater SM5, whose Zn composition indicates that it likely suffered from terrestrial contamination, Si composes at least 7.2 atom% of all micron-scale crater residues and 4.9 atom% of all observed submicron crater residues. Mg was also observed in all craters, though it is missing from some residue subregions. Mg abundances are typically slightly lower than Si abundances in the craters. Mg/Si ratios range from 0.68 to 1.10 in the bulk micron-scale crater compositions and Mg abundances range from 0.4 to 4.3 atom% in the submicron craters. Definitively identifying the silicate impactors is difficult. Our cross section thicknesses range from 100 to 150 nm while individual subgrains in the impacting aggregates are likely smaller, making the isolation of any individual impactor challenging. Additionally, our crater residues are amorphous, meaning that any grains present in the original impactor have likely mixed with other subgrains composing the aggregate. Pyroxene and olivine are potential components of the impactors but cannot fully explain the observed elemental abundances. O/Si ratios in the micron-scale residue layers range from 4.9 to 10.0 and are too high for pyroxene or olivine to be the sole O sources. O/Si ratios in craters SM6, SM7, SM9, and SM10 similarly are not stoichiometrically consistent with olivine and pyroxene, with O/Si ratios largely falling between 4.0 and 7.5. O overabundances in some regions may also be the result of surface-oxidized Al from the foils mixing with the impactor residues. Previous analog foil experiments have not observed preferential loss of Si, Mg, or Fe relative to O in olivine and diopside impactors, indicating the loss of cations in the impactors may be unlikely (Wozniakiewicz et al. 2012b). However, these experiments were conducted using crystalline precursors, and cation loss may be more likely in amorphous precursors. O/Si values in chondrites are largely influenced by the oxidation state of Fe, and O/Si values can reach 7.9 for CI chondrites containing hydrated silicates, carbonates, and sulfates (Mason 1979). O overabundances can also be explained by oxygen-rich species such as iron oxides constituting a fraction of the impactor material. O/Si ratios observed in IDPs frequently range from 4.0 to 6.0, allowing IDP

components such as GEMS to be a potential contributor to the O and Si observed in our residues (Schramm et al. 1989). However, while GEMS can have Mg/Si ratios as low as 0.05, they are typically more Mg-rich than our submicron residues with average Mg/Si ratios close to 0.67 (Keller and Messenger 2011).

Iron sulfide residues are ubiquitous within our craters. Fe/S ratios range between 1.6 and 4.2 in the micron-scale craters and 0.67–3.05 in the submicron craters. The majority of Fe/S ratios are greater than 1.0, indicating that S loss, which is common in analog foil experiments, may have occurred (Wozniakiewicz et al. 2011). However, given the ubiquitous presence of Si in our residues, some Fe may have been contributed by silicate impactors (e.g., Fe-rich olivine) that would lead to Fe/S ratios greater than 1.0. Fe may also have been contributed by iron oxides or metals, which have previously been observed in Wild 2 materials (Westphal et al. 2009). Some Fe in the micron-scale foils may also have been contributed by Fe impurities (e.g., Fig. 2c) known to exist within the Stardust foils (Kearsley et al. 2007). Ni abundances in craters M3, SM6, SM9, and SM10 are too high relative to the Fe abundances in the craters for pyrrhotite or troilite alone to be responsible for the observed Fe and S. The Fe/Ni ratios in these craters range from 5.54 to 14.4 while pyrrhotite reported in GEMS grains, although capable of having similarly low Fe/Ni ratios, largely have Fe/Ni ratios of 15.7 or higher (Bradley and Dai 2004; Keller and Messenger 2011). Additionally, crater M4 contained discrete Ni hot spots associated with large Fe and S abundances. Our Ni abundances in these craters can be explained by a minor fraction of pentlandite among pyrrhotite and troilite impacting materials.

Although individually the O-Si-Mg and Fe-S-Ni components of these craters can be explained by GEMS impactors, the ratios of these two components cannot. Fe/Si ratios in GEMS have been observed to range from 0.09 up to 1.63 with an average of 0.56 (Keller and Messenger 2011). Craters M3 and M4 have Fe/Si ratios larger than 2.2, and craters SM5, SM6, and SM7 have no regions where Fe/Si ever falls below 2.04. Craters SM9 and SM10, though containing subregions with Fe/Si ratios ranging between 0.26 and 0.72, both have average Fe/Si ratios that fall above reported Fe/Si ratios for GEMS. While GEMS grains could potentially represent a component of our impactors, our crater residues are too heavily dominated by iron-nickel sulfide residues to have been sourced entirely from GEMS. Similarly, while our Si/Fe ratios fall within the range of values seen within IDPs, our craters are more Si-depleted compared to the majority of reported Si/Fe values seen in IDPs (Schramm et al. 1989).

Zn Abundances in the Submicron Craters

Zn is abundant in our submicron crater residues and appears in all submicron craters containing a residue layer. Crater SM8, which did not contain a residue layer, had no Zn signature, demonstrating that our observed Zn peaks in the EDS spectra are not the result of instrumental bias. S was also present in each submicron crater's residue, and Craters SM7, SM9, and SM10 all contain subregions with Fe/S ratios less than 1, allowing for zinc sulfides to be a potential source of both the Zn and abundant S in these subregions. S loss within the foils is also expected due to the high collection velocity, allowing for zinc sulfides as a possibility even within regions with (Zn+Fe)/S ratios greater than 1 (Wozniakiewicz et al. 2011). Zinc sulfides have been observed in previous FIB-TEM investigations of Stardust foil craters (Leroux et al. 2008a). Zinc sulfides have also been observed in the form of Fe-rich sphalerite in both IDPs (Christoffersen and Buseck 1986; Rietmeijer 1998) as well as Stardust aerogel tracks (Zolensky et al. 2006). Current estimates suggest over 85% of stratospheric IDPs originated from comets (Nesvorny et al. 2010). If these estimates are accurate, zinc sulfides are likely a component of Wild 2's fine grains. Cubanite ($CuFe_2S_3$) has been observed in the Stardust aerogels as well (Berger et al. 2011) demonstrating that Wild 2 contains sulfides with a variety of chalcophilic elements.

While Zn concentrations are sufficiently low in craters SM6, SM7, SM9, and SM10 to be explained as the remains of impacting zinc sulfides, crater SM5 had extremely large Zn abundances with Zn reaching values as high as 63 atom% in subregions of the crater (Fig. 16; Table 3). Additionally, Zn abundances in crater SM5 are anti-correlated with S abundances within the crater residue. Zn observations in the Stardust interstellar foils have frequently been tied to secondary impacts from cover glass present on the Stardust spacecraft solar cells (Stroud et al. 2014). While traces of K were observed throughout the crater, which is also a component of the solar cell cover glass, Zn is only believed to compose a small fraction of the cover glass (3–4 wt%; Stroud et al. 2014), making the cover glass an unlikely source for the crater's Zn. Other components of the spacecraft may have higher Zn abundances than the solar cell cover glass, though the composition of much of the Stardust spacecraft remains proprietary information. However, the presence of Si, Mg, Fe, and S imply that some portion of the crater residue is cometary, and secondary impacts on the Stardust interstellar foils have not appeared to be combinations of both cometary and spacecraft material (Stroud et al. 2014). The crater's morphology, indicative of an impactor that was moving roughly perpendicular to the sample collector, also does not support a secondary impact from the spacecraft itself. Another possibility is that the Zn is the result of terrestrial contamination. Bulk measurements have shown that Zn is a low-level contaminant of the Stardust foils (~75 ppm; Kearsley et al. 2007). However, it is not known whether the Zn is evenly distributed throughout the foils or if it appears as discrete Zn-rich inclusions similar to Fe-rich inclusions more commonly seen in the foils (Kearsley et al. 2007). Impact with a discrete Zn-rich inclusion could potentially lead to the high Zn abundances that we observe.

Zn, though present in IDPs and collected Wild 2 materials, is not frequently a component of these materials. Nonrandom impact distributions within the Stardust cometary collector could potentially explain the presence of Zn in each of our craters, which were only spread across a region of 5.28 mm^2. Clustering does appear in the Stardust collection media, with the most statistically significant results occurring on scales smaller than ~10 cm (Westphal et al. 2008). However, no hypothesis fully explains the observed clustering, making it difficult to assess why Zn was present throughout our crater residues. Zn's presence throughout our craters may also be the result of our study's small sample size, and further studies of the Stardust submicron impactors are necessary to accurately characterize the Zn component of the Wild 2 fine grains.

Ca Abundances

Ca is present in small quantities (0.2–3.4 atom%) in the micron-scale craters and four of five submicron craters. The source of this Ca is difficult to determine. Calcium-aluminum-rich inclusions (CAIs) have been found in the Stardust sample collector (Brownlee et al. 2006; Joswiak et al. 2017). Traces (<1 atom%) of Ti are present in all of our micron-scale craters, and Ti is also present in craters SM7 and SM10. Ti in these crater residues is indicative of potential CAI impactors. Fassaite ($Ca[Mg,Ti,Al][Si,Al]_2O_6$) and nanocrystalline osbornite ($Ti[V]N$) have both been observed in Stardust-collected CAIs (Chi et al. 2009). However, the Ti detected in the micron-scale craters may be the result of Ti present in the STEM sample holder, and ubiquitous Al contamination makes positive identification of CAIs in the foil samples difficult.

Kosmochloric Ca-rich pyroxene and olivine (Kool) grains have been commonly observed in Stardust aerogels as a source of cometary Ca (Joswiak et al. 2009). Trace (<0.5 atom%) K and Cr was present in craters M1 and M3, indicating that fractions of the impacting material may have been composed of Kool grains. However, our submicron craters had low Mg abundances as well as low Cr abundances and a lack of

Na, suggesting an alternate source for the Ca observed in our submicron craters.

Pyroxene grains are the most likely source for the observed Ca. Pyroxene grains have previously been observed and linked with Ca abundances in Stardust foil residues (Leroux et al. 2008a), and low-Ca pyroxenes are common in the Stardust aerogel tracks (Jacob et al. 2009). Although the O/Si ratios are inconsistent with pyroxene as a whole in many of our craters, Si, O, and Ca abundances allow for a portion of these elements to have been contributed by Ca-containing pyroxene impactors. Ca concentrations in the micron-scale craters and submicron craters M6, M9, and M10 are low enough to have been fully contributed by low-Ca pyroxenes. Craters SM5 and SM9 have Ca/Si ratios greater than 0.2 and would require higher Ca pyroxene impactors (e.g., pigeonite) that appear less commonly in the Stardust aerogel tracks (Jacob et al. 2009).

Refractory Materials in the Micron-Scale Craters

Micron-scale crater M2 contains Mg- and O-rich subregions consistent with contributions from a spinel impactor (Fig. 5; Table 2). A lack of crystallographic data as well as accurate Al abundance measurements prevent definitive identification of the impactor as spinel. However, the Mg/Si ratios in these regions are too large to be stoichiometrically consistent with other common Mg-rich impactors such as olivine and pyroxene. Spinel grains on the scale of several hundred nanometers have been identified in Stardust aerogel tracks (Simon et al. 2008), but spinel has not been observed in micron-scale or submicron Stardust foil craters (Leroux et al. 2008a, 2010; Stroud et al. 2010).

Micron-scale crater M1 has discrete Ni-rich regions that are not associated with increased S abundance (Fig. 4; Table 2). As a result, these regions are unlikely to be the result of iron-nickel sulfides without assuming excessive S-loss that is uncharacteristic of the other measured iron sulfide residues in the crater. Taenite is consistent with the observed Fe and Ni abundances in the crater residues. Taenite has previously been observed in studies of the Stardust aerogels (Leroux et al. 2008b), but not in Stardust craters on our size scales (Leroux et al. 2008a, 2010; Stroud et al. 2010). Cr in the craters may have been contributed by Kool grains (Joswiak et al. 2009), but may also be the result of chromite impactors. Chromite has previously been observed in a submicron Stardust crater (Stroud et al. 2010), demonstrating that it is a component of the Wild 2 fines.

Spinel, taenite, chromite, and CAIs are all fairly refractory materials. Spinel and chromite have melting temperatures exceeding 2400 K, and CAIs are among the first materials to have formed in the early solar system. The presence of spinel and taenite in the micron-scale craters, as well as the potential for chromite and CAI impactors, indicates that refractory materials are fairly common components of micron-scale impactors on the Stardust foils. We did not observe evidence for similarly refractory materials in our submicron impactors. As a result, the abundance of refractory inclusions may be a way to differentiate Wild 2 particles on the scale of several hundred nanometers from particles closer to a micron in size. However, additional studies of the Stardust foils are required to verify whether refractory composition is dependent on impactor sizes at these scales.

Bulk Crater Compositions

Our average crater residue compositions for the micron-scale craters and submicron craters SM6, SM7, SM9, and SM10 are shown in Fig. 17 with our values normalized to Si and CI chondrite abundances (Lodders 2003). We also compare our results to CP IDPs (Schramm et al. 1989), though Schramm et al. (1989) acknowledged that a significant fraction of their measured Si may be caused by silicon oil contamination from the IDP collection process, which would depress element/Si ratios. Overall our crater residues are Si- and Mg-poor relative to CI chondrites causing our craters to appear enriched in Fe, Ni, and S with the submicron craters also appearing heavily enriched in Zn. Our craters also contained a higher proportion of iron-nickel sulfide residues and zinc sulfide residues relative to silicates when compared to CP IDPs. Zn was the most abundant element in our submicron crater residues relative to CI chondrite abundances, with Zn/Si ratios normalized to CI abundances ranging from 64.0 to 1440.5 in submicron craters SM6, SM7, SM9, and SM10. S is the second most abundant element in the submicron crater residues relative to CI chondrite abundances, with S/Si ratios normalized to CI abundances ranging from 2.9 to 6.7. Given the potential loss of volatiles during the capture process, the impactors' Zn and S abundances may have been higher than measured (Wozniakiewicz et al. 2011). The micron-scale craters showed significantly less volatile element enrichment. Only micron-scale crater M4 had an S/Si ratio normalized to CI abundances larger than 1.3, and no Zn was detected in the micron-scale craters.

Reports on S abundances in Wild 2 material have differed. Flynn et al. (2006) studied full aerogel tracks (lengths of 250–10,000 μm) and large foil craters (diameters of 57–238 μm) and observed that S was depleted relative to CI values whereas the chalcophilic elements Cu, Ga, and Zn were enriched. However, the majority of the studied Wild 2 mass originated from larger impactors. Westphal et al. (2009) studied fragments in Stardust aerogel tracks and observed an
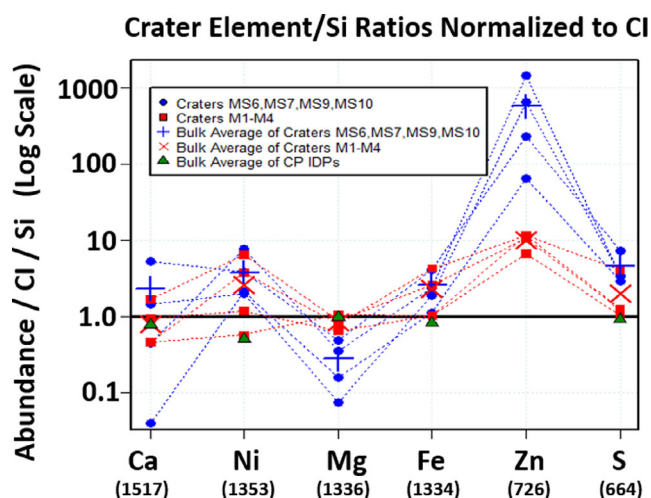
Fig. 17. Element/Si ratios observed in the micron-scale craters (M1–M4) and submicron craters SM6, SM7, SM9, and SM10 plotted logarithmically with results normalized to CI chondrite values (Lodders 2003). Values for the submicron craters were calculated by summing each crater subregions' composition. Zn values for the micron-scale craters were calculated using an upper limit of 1 atom% Zn as Zn was not detected in these craters during our study. Lines connect measurements from the same crater. The bulk averages of the craters, corrected for crater sizes, are also shown. Elements are listed in order of decreasing 50% condensation temperature, listed in parentheses in Kelvin below each element (Lodders 2003). Also shown are values from CP IDPs (Schramm et al. 1989) excluding Zn as Zn was not detected in the cited study. CI values are represented by the horizontal black line. The submicron craters showed significant enrichment in the volatile elements S and Zn relative to the micron-scale craters. (Color figure can be viewed at wileyonlinelibrary.com.)

excess of Fe bound as iron sulfides compared to other major meteorite groups and no overall S depletions. However, the Westphal et al. (2009) measurements were bulk track measurements, mostly dominated by large terminal fragments.

Our measurements of high Zn and S in the submicron Wild 2 impactors suggest that the submicron impactors may be fundamentally different from the larger micron-scale impactors. The high Zn and S abundances in the submicron Wild 2 impactors also support the hypothesis that Wild 2 fine material is not depleted in the moderately volatile elements relative to the bulk solar system abundances. While the sample size is small, our crater compositions suggest that the fine component of Wild 2 is fundamentally different from its coarse component. Wild 2's coarse components typically have high-temperature origins and volatile element depletions, and appear to have formed far from where the parent body accreted (Brownlee et al. 2012). The small cometary impactors that produced the submicron craters that we studied appear to be enriched in moderately volatile elements and likely did not

have an igneous origin. However, our craters constitute only a fraction of the collected Wild 2 fines and a more comprehensive analysis of the fine impactors is necessary to fully characterize their volatile components. Zn is not common in the Wild 2 samples, and the ubiquitous Zn in our submicron craters may be the result of impact clustering (Westphal et al. 2008) of sulfide-rich or Si-depleted materials, resulting in a sample that is not truly representative of the Wild 2 fine component. Further analysis of the submicron craters on the Stardust foils is necessary to better characterize the volatile components of fine-grained Wild 2 material and to see if our observed trend of volatile enrichment continues.

CONCLUSIONS

We extracted four micron-scale (1.8–5.2 μm) and six (220–380 nm) submicron impact craters from Stardust foil C2113N-A, and studied them with FIB-TEM techniques. One submicron crater (SM5) was contaminated with a likely terrestrial source of Zn, and another submicron crater (SM8) lacked any impactor residue. The remaining craters contained residue layers dominated by a combination of silicate and sulfide impactors.

Our crater residues, though potentially partially composed of GEMS materials, cannot be composed entirely of GEMS grains given our low amounts of Si and Mg relative to iron-nickel sulfide and zinc sulfide components (Keller and Messenger 2011). Our submicron crater residues contain materials found in IDPs such as zinc sulfides, but are more sulfur rich than the majority of studied IDPs (Schramm et al. 1989).

Several micron-scale crater residues appeared to be derived from spinel and taenite impactors. These craters also contained Cr, Ca, and Ti, potentially indicating the presence of chromite and CAIs, both of which have previously been observed in comet Wild 2 samples. The presence of these refractory materials differentiated the micron-scale craters from our submicron craters, which did not appear to contain similarly refractory materials. As a result, refractory material abundances may differentiate Wild 2 dust on the scale of several hundred nanometers from larger particles on the scale of a micron, but further analysis of the Stardust fine component is necessary to verify this hypothesis.

The submicron crater residues, excluding the contaminated crater SM5, are enriched in S and Zn when normalized to Si and CI chondrite abundances. Although this study is a small sample size and may not be representative of the bulk comet, the material's enrichment in moderately volatile elements in the small-crater residue studied so far suggests that the Wild 2 fines did not form by igneous processes, distinguishing the comet's fine component from the large terminal

particles which mostly formed by high-temperature events.

Further investigation of submicron craters on the Stardust foils will aid in determining the bulk composition of the Wild 2 fine component with better statistical precision. A robust characterization of the Wild 2 fines, particularly the volatiles, would help to determine the provenance of primordial dust in the solar system.

Editorial Handling—Dr. Alexander Ruzicka

REFERENCES

Berger E. L., Zega T. J., Keller L. P., and Lauretta D. S. 2011. Evidence for aqueous activity on comet 81P/Wild 2 from sulfide mineral assemblages in Stardust samples and CI chondrites. *Geochimica et Cosmochimica Acta* 75:3501–3513.

Bradley J. P. and Dai Z. R. 2004. Mechanism of formation of glass with embedded metal and sulfides. *The Astrophysical Journal* 617:650–655.

Brownlee D., Hörz F., Newburn R. L., Zolensky M. E., Duxbury T. C., Sandford S., Sekanina Z., Tsou P., Hanner M. S., Clark B. C., Green S. F., and Kissel J. 2004. Surface of young Jupiter family comet 81P/Wild 2: View from the Stardust spacecraft. *Science* 304:1764–1769.

Brownlee D., Tsou P., Aléon J., Alexander C. M. O'D., Araki T., Bajt S., Baratta G. A., Bastien R., Bland P., Bleuet P., Borg J., Bradley J. P., Brearley A., Brenker F., Brennan S., Bridges J. C., Browning N. D., Brucato J. R., Bullock E., Burchell M. J., Busemann H., Butterworth A., Chaussidon M., Cheuvront A., Chi M., Cintala M. J., Clark B. C., Clemett S. J., Cody G., Colangeli L., Cooper G., Cordier P., Daghlian C., Dai Z., D'Hendecourt L., Djouadi Z., Dominguez G., Duxbury T., Dworkin J. P., Ebel D. S., Economou T. E., Fakra S., Fairey S. A. J., Fallon S., Ferrini G., Ferroir T., Fleckenstein H., Floss C., Flynn G., Franchi I. A., Fries M., Gainsforth Z., Gallien J.-P., Genge M., Gilles M. K., Gillet Ph., Gilmour J., Glavin D. P., Gounelle M., Grady M. M., Graham G. A., Grant P. G., Green S. F., Grossemy F., Grossman L., Grossman J. N., Guan Y., Hagiya K., Harvey R., Heck P., Herzog G. F., Hoppe P., Hörz F., Huth J., Hutcheon I. D., Ignatyev K., Ishii H., Ito M., Jacob D., Jacobsen C., Jacobsen S., Jones S., Joswiak D., Jurewicz A., Kearsley A. T., Keller L. P., Khodja H., Kilcoyne A. L. D., Kissel J., Krot A., Langenhorst F., Lanzirotti A., Le L., Leshin L. A., Leitner J., Lemelle L., Leroux H., Liu M.-C., Luening K., Lyon I., MacPherson G., Marcus M. A., Marhas K., Marty B., Matrajt G., McKeegan K., Meibom A., Mennella V., Messenger K., Messenger S., Mikouchi T., Mostefaoui S., Nakamura T., Nakano T., Newville M., Nittler L. R., Ohnishi I., Ohsumi K., Okudaira K., Papanastassiou D. A.,

Palma R., Palumbo M. E., Pepin R. O., Perkins D., Perronnet M., Pianetta P., Rao W., Rietmeijer F. J. M., Robert F., Rost D., Rotundi A., Ryan R., Sandford S. A., Schwandt C. S., See T. H., Schlutter D., Sheffield-Parker J., Simionovici A., Simon S., Sitnitsky I., Snead C. J., Spencer M. K., Stadermann F. J., Steele A., Stephan T., Stroud R., Susini J., Sutton S. R., Suzuki Y., Taheri M., Taylor S., Teslich N., Tomeoka K., Tomioka N., Toppani A., Trigo-Rodríguez J. M., Troadec D., Tsuchiyama A., Tuzzolino A. J., Tyliszczak T., Uesugi K., Velbel M., Vellenga J., Vicenzi E., Vincze L., Warren J., Weber I., Weisberg M., Westphal A. J., Wirick S., Wooden D., Wopenka B., Wozniakiewicz P., Wright I., Yabuta H., Yano H., Young E. D., Zare R. N., Zega T., Ziegler K., Zimmermann L., Zinner E., and Zolensky M. 2006. Comet 81P/Wild 2 under a microscope. *Science* 314:1711–1716.

Brownlee D., Joswiak D., and Matrajt G. 2012. Overview of the rocky component of Wild 2 comet samples: Insight into the early solar system, relationship with meteoritic materials and the differences between comets and asteroids. *Meteoritics & Planetary Science* 47:453–470.

Burchell M. J., Fairey S. A., Wozniakiewicz P., Brownlee D. E., Hörz F., Kearsley A. T., See T. H., Tsou P., Westphal A., Green S. F., Trigo-Rodríguez J. M., and Domínguez G. 2008. Characteristics of cometary dust tracks in Stardust aerogel and laboratory calibrations. *Meteoritics & Planetary Science* 43:23–40.

Chi M., Ishii H. A., Simon S. B., Bradley J. P., Dai Z. R., Joswiak D. J., Browning N. D., and Matrajt D. 2009. The origin of refractory minerals in comet 81P/Wild 2. *Geochimica et Cosmochimica Acta* 73:7150–7161.

Christoffersen R. and Buseck P. R. 1986. Mineralogy of interplanetary dust particles from the "olivine" infrared class. *Earth & Planetary Science Letters* 78:53–66.

Croat T. K., Floss C., Haas B. A., Burchell M., and Kearsley A. T. 2015. Survival of refractory presolar grain analogs during Stardust-like impact into Al foils: Implications for Wild 2 presolar grain abundances and study of the cometary fine fraction. *Meteoritics & Planetary Science* 50:1378–1391.

Flynn G. J., Bleuet P., Borg J., Bradley J. P., Brenker F. E., Brennan S., Bridges J., Brownlee D. E., Bullock E. S., Burghammer M., Clark B. C., Dai Z. R., Daghlian C. P., Djouadi Z., Fakra S., Ferroir T., Floss C., Franchi I. A., Gainsforth Z., Gallien J.-P., Gillet P., Grant P. G., Graham G. A., Green S. F., Grossemy F., Heck P. R., Herzog G. F., Hoppe P., Horz F., Huth J., Ignatyev K., Ishii H. A., Janssens K., Joswiak D., Kearsley A. T., Khodja H., Lanzirotti A., Leitner J., Lemelle L., Leroux H., Luening K., MacPherson G. J., Marhas K. K., Marcus M. A., Matrajt G., Nakamura T., Nakamura-Messenger K., Nakano T., Newville M., Papanastassiou D. A., Pianetta P., Rao W., Riekel C., Rietmeijer F. J. M., Rost D., Schwandt C. S., See T. H., Sheffield-Parker J., Simionovici A., Sitnitsky I., Snead C. J., Stadermann F. J., Stephan T., Stroud R. M., Susini J., Suzuki Y., Sutton S. R., Taylor S., Teslich N., Troadec D., Tsou P., Tsuchiyama A., Uesugi K., Vekemans B., Vicenzi E. P., Vincze L., Westphal A. J., Wozniakiewicz P., Zinner E., and Zolensky M. E. 2006. Elemental compositions of comet 81P/Wild 2 samples collected by Stardust. *Science* 314:1731–1735.

Hanner M. S. 2003. The mineralogy of cometary dust. In *Astromineralogy*, edited by Henning T. New York: Springer. pp. 171–188.

Hörz F., Bastien R., Borg J., Bradley J. P., Bridges J. C., Brownlee D. E., Burchell M. J., Chi M., Cintala M. J., Dai Z. R., Djouadi Z., Dominguez G., Economou T. E., Fairey S. A. J., Floss C., Franchi I. A., Graham G. A., Green S. F., Heck P., Hoppe P., Huth J., Ishii H., Kearsley A. T., Kissel J., Leitner J., Leroux H., Marhas K., Messenger K., Schwandt C. S., See T. H., Snead C., Stadermann F. J., Stephan T., Stroud R., Teslich N., Trigo-Rodríguez J. M., Tuzzolino A. J., Troadec D., Tsou P., Warren J., Westphal A., Wozniakiewicz P., Wright I., and Zinner E. 2006. Impact features on stardust: Implications for comet 81P/Wild 2 dust. *Science* 314:1716–1719.

Ishii H. A. 2019. Comparison of GEMS in interplanetary dust particles and GEMS-like objects in a Stardust impact track in aerogel. *Meteoritics & Planetary Science* 54:202–219.

Ishii H. A., Bradley J. P., Dai Z. R., Chi M. F., Kearsley A. T., Burchell M. J., Browning N. D., and Molster F. 2008. Comparison of comet 81P/Wild 2 dust with interplanetary dust from comets. *Science* 319:447–450.

Jacob D., Stodolna J., Leroux H., Langenhorst F., and Houdellier F. 2009. Pyroxenes microstructure in comet 81P/Wild 2 terminal Stardust particles. *Meteoritics & Planetary Science* 44:1475–1488.

Joswiak D. J., Brownlee D. E., Matrajt G., Westphal A. J., and Snead C. J. 2009. Kosmochloric Ca-rich pyroxenes and FeO-rich olivines (Kool grains) and associated phases in Stardust tracks and chondritic porous interplanetary dust particles: Possible precursors to FeO-rich type II chondrules in ordinary chondrites. *Meteoritics & Planetary Science* 44:1561–1588.

Joswiak D. J., Brownlee D. E., Nguyen A. N., and Messenger S. 2017. Refractory materials in comet samples. *Meteoritics & Planetary Science* 52:1612–1648.

Kearsley A. T., Burchell M. J., Hörz F., Cole M. J., and Schwandt C. S. 2006. Laboratory simulation of impacts on aluminum foils of the Stardust spacecraft: Calibration of dust particle size from comet Wild-2. *Meteoritics & Planetary Science* 41:167–180.

Kearsley A. T., Graham G. A., Burchell M. J., Cole M. J., Dai Z. R., Teslich N., Bradley J. P., Chater R., Wozniakiewicz P. A., Spratt J., and Jones G. 2007. Analytical scanning and transmission electron microscopy of laboratory impacts on Stardust aluminum foils: Interpreting impact crater morphology and the composition of impact residues. *Meteoritics & Planetary Science* 42:191–210.

Kearsley A. T., Borg J., Graham G. A., Burchell M. J., Cole M. J., Leroux H., Bridges J. C., Hörz F., Wozniakiewicz P. J., Bland P. A., Bradley J. P., Dai Z. R., Teslich N., See T., Hoppe P., Heck P. R., Huth J., Stadermann F. J., Floss C., Marhas K., Stephan T., and Leitner J. 2008. Dust from comet Wild 2: Interpreting particle size, shape, structure, and composition from impact features on the Stardust aluminum foils. *Meteoritics & Planetary Science* 43:41–73.

Keller L. P. and Messenger S. 2011. On the origins of GEMS grains. *Geochimica et Cosmochimica Acta* 75:5336–5365.

Komatsu M., Fagan T. J., Mikouchi T., Petaev M. I., and Zolensky M. E. 2015. LIME silicates in amoeboid olivine aggregates in carbonaceous chondrites: Indicator of nebular and asteroidal processes. *Meteoritics & Planetary Science* 50:1271–1294.

Leroux H., Stroud R. M., Dai Z. R., Graham G. A., Troadec D., Bradley J. P., Teslich N., Borg J., Kearsley A. T., and Hörz F. 2008a. Transmission electron microscopy of cometary residues from micron-sized craters in the Stardust Al foils. *Meteoritics & Planetary Science* 43:143–160.

Leroux H., Rietmeijer F. J. M., Velbel M. A., Brearley A. J., Jacob D., Langenhorst F., Bridges J. C., Zega T. J., Stroud R. M., Cordier P., Harvey R. P., Lee M., Gounelle M., and Zolensky M. E. 2008b. A TEM study of thermally modified comet 81P/Wild 2 dust particles by interactions with the aerogel matrix during the Stardust capture process. *Meteoritics & Planetary Science* 43:97–120.

Leroux H., Kearsley A. T., and Troadec D. 2010. Mineralogy of Wild 2 residues in micron-sized craters from the Stardust Al-foils (abstract #1621). 41st Lunar and Planetary Science Conference. CD-ROM.

Lodders K. 2003. Solar system abundances and condensation temperatures of the elements. *The Astrophysical Journal* 591:1220–1247.

Mason B. 1979. Data of geochemistry, Chapter B. Cosmochemistry. In *Geological Survey Professional Paper 440-B-1*. Washington, D.C.: U.S. Government Printing Office. 132 pp.

Nesvorny D., Jenniskens P., Levison H. F., Bottke W. F., Vokrouhlický D., and Gounelle M. 2010. Cometary origin of the zodiacal cloud and carbonaceous micrometeorites. Implications for hot debris disks. *The Astrophysical Journal* 713:816–836.

Ogliore R. C., Nagashima K., Huss G. R., Westphal A. J., Gainsforth Z., and Butterworth A. L. 2015. Oxygen isotopic composition of coarse- and fine-grained material from comet 81P/Wild 2. *Geochimica et Cosmochimica Acta* 166:74–91.

Price M. C., Kearsley A. T., Burchell M. J., Hörz F., Borg J., Bridges J. C., Cole M. J., Floss C., Graham G., Green S. F., Hoppe P., Leroux H., Marhas K. K., Park N., Stroud R., Stadermann F. J., Telisch N., and Wozniakiewicz P. J. 2010. Comet 81P/Wild 2: The size distribution of finer (sub-10 µm) dust collected by the Stardust spacecraft. *Meteoritics & Planetary Science* 45:1409–1428.

Rietmeijer F. J. M. 1998. Interplanetary dust particles. In *Planetary materials*, edited by Papike J. J. Reviews in Mineralogy, vol. 36. Chantilly, Virginia: Mineralogical Society of America. pp. 2-1–2-95.

Ritchie N. W. M. 2011. Standards-based quantification in DTSA-II — Part I. *Microscopy Today* 19:30–36.

Ritchie N. W. M. 2012. Standards-based quantification in DTSA-II — Part II. *Microscopy Today* 20:24–28.

Schramm L. S., Brownlee D. E., and Wheelock M. M. 1989. Major element composition of stratospheric micrometeorites. *Meteoritics* 24:99–112.

Simon S. B., Joswiak D. J., Ishii H. A., Bradley J. P., Chi M., Grossman L., Aléon J., Brownlee D. E., Fallon S., Hutcheon I. D., Matrajt G., and McKeegan K. D. 2008. A refractory inclusion returned by Stardust from comet 81P/Wild 2. *Meteoritics & Planetary Science* 43:1861–1877.

Stodolna J., Jacob D., and Leroux H. 2012. Mineralogy and petrology of Stardust particles encased in the bulb of track 80: TEM investigation of the Wild 2 fine-grained material. *Geochimica et Cosmochimica Acta* 87:35–50.

Stroud R. M., Koch I. M., Bassim N. D., Piccard Y. N., and Nittler L. R. 2010. Structure and composition of comet Wild 2 residues in sub-micron to micron-sized craters (abstract #1792). 41st Lunar and Planetary Science Conference. CD-ROM.

Stroud R. M., Allen C., Ansari A., Anderson D., Bajt S.,
Bassim N., Bastien R. S., Bechtel H. A., Borg J., Brenker F.
E., Bridges J., Brownlee D. E., Burchell M., Burghammer
M., Butterworth A. L., Changela H., Cloetens P., Davis A.
M., Doll R., Floss C., Flynn C. G., Frank D. R.,
Gainsforth Z., Grün E., Heck P. R., Hillier J. K., Hoppe P.,
Huth J., Hvide B., Kearsley A., King A. J., Kotula P., Lai
B., Leitner J., Lemelle L., Leroux H., Leonard A., Lettieri
R., Marchant W., Nittler L. R., Ogliore R., Ong W. J.,
Postberg F., Price M. C., Sandford S. A., Tresseras J.-A. S.,
Schmitz S., Schoonjans T., Schreiber K., Silversmit G.,
Simionovici A. S., Solé V. A., Srama R., Stephan T.,
Sterken V. J., Stodolna J., Sutton S., Trieloff M., Tsou P.,
Tsuchiyama A., Tyliszczak T., Vekemans B., Vincze L.,
Westphal A. J., Von Korff J., Zevin D., and Zolensky M. E.
2014. Stardust interstellar preliminary examination XI:
Identification and elemental analysis of impact craters on Al
foils from the Stardust Interstellar Dust Collector.
Meteoritics & Planetary Science 49:1698–1719.
Tsou P., Brownlee D. E., Anderson J. D., Bhaskaran S.,
Cheuvront A. R., Clark B. C., Duxbury T., Economou T.,
Green S. F., Hanner M. S., Hörz F., Kissel J., McDonnell
A. M., Newburn R. L., Ryan R. E., Sandford S. A.,
Sekanina Z., Tuzzolino A. J., Vellinga J. M., and
Zolensky M. E. 2004. Stardust encounters comet 81P/Wild
2. *Journal of Geophysical Research* 109:1–8.
Westphal A. J., Bastien R. K., Borg J., Bridges J., Brownlee
D. E., Burchell M. J., Cheng A. F., Clark B. C., Djouadi
Z., Floss C., Franchi I., Gainsforth Z., Graham G., Green
S. F., Heck P. R., Horányi M., Hoppe P., Hörz F. P.,
Huth J., Kearsley A., Leroux H., Marhas K., Nakamura-
Messenger K., Sandford S. A., See T. H., Stadermann F.
J., Teslich N. E., Tsitrin S., Warren J. L., Wozniakiewicz
P. J., and Zolensky M. E. 2008. Discovery of non-random
spatial distribution of impacts in the Stardust cometary
collector. *Meteoritics & Planetary Science* 43:415–429.
Westphal A. J., Fakra S. C., Gainsforth Z., Marcus M. A.,
Ogliore R. C., and Butterworth A. L. 2009. Mixing
fraction of inner solar system material in comet 81P/Wild
2. *The Astrophysical Journal* 694:18–28.
Wozniakiewicz P. J., Ishii H. A., Kearsley A. T., Burchell M.
J., Bland P. A., Bradley J. P., Dai Z., Teslich N., Collins
G. S., Cole M. J., and Russell S. S. 2011. Investigation of

iron sulfide impact crater residues: A combined analysis by
scanning and transmission electron microscopy.
Meteoritics & Planetary Science 46:1007–1027.
Wozniakiewicz P. J., Kearsley A. T., Ishii H. A., Burchell M.
J., Bradley J. P., Teslich N., Cole M. J., and Price M. C.
2012a. The origin of crystalline residues in Stardust Al
foils: Surviving cometary dust or crystallized impact melts?
Meteoritics & Planetary Science 47:660–670.
Wozniakiewicz P. J., Ishii H. A., Kearsley A. T., Burchell M.
J., Bradley J. P., Price M. C., Teslich N., Lee M. R., and
Cole M. J. 2012b. Stardust impact analogs: Resolving pre-
and postimpact mineralogy in Stardust Al foils.
Meteoritics & Planetary Science 47:708–728.
Zolensky M. E., Zega T. J., Yano H., Wirick S., Westphal A.
J., Weisberg M. K., Weber I., Warren J. L., Velbel M. A.,
Tsuchiyama A., Tsou P., Toppani A., Tomioka N.,
Tomeoka K., Teslich N., Taheri M., Susini J., Stroud R.,
Stephan T., Stadermann F. J., Snead C. J., Simon S. B.,
Simionovici A., See T. H., Robert F., Rietmeijer F. J. M.,
Rao W., Perronnet M. C., Papanastassiou D. A.,
Okudaira K., Ohsumi K., Ohnishi I., Nakamura-
Messenger K., Nakamura T., Mostefaoui S., Mikouchi T.,
Meibom A., Matrajt G., Marcus M. A., Leroux H.,
Lemelle L., Le L., Lanzirotti A., Langenhorst F., Krot A.
N., Keller L. P., Kearsley A. T., Joswiak D., Jacob D.,
Ishii H., Harvey R., Hagiya K., Grossman L., Grossman
J. N., Graham G. A., Gounelle M., Gillet P., Genge M. J.,
Flynn G., Ferroir T., Fallon S., Ebel D. S., Dai Z. R.,
Cordier P., Clark B., Chi M., Butterworth A. L., Brownlee
D. E., Bridges J. C., Brennan S., Brearley A., Bradley J.
P., Bleuet P., Bland P. A., and Bastien R. 2006.
Mineralogy and petrology of comet 81P/Wild 2 nucleus
samples. *Science* 314:1735–1739.
Zolensky M., Nakamura-Messenger K., Rietmeijer F.,
Leroux H., Mikouchi T., Ohsumi K., Simon S.,
Grossman L., Stephan T., Weisberg M., Velbel M.,
Zega T., Stroud R., Tomeoka K., Ohnishi I., Tomioka
N., Nakamura T., Matrajt G., Joswiak D., Brownlee D.,
Langenhorst F., Krot A., Kearsley A., Ishii H., Graham
G., Dai Z. R., Chi M., Bradley J., Hagiya K., Gounelle
M., Keller L., and Bridges J. 2008. Comparing Wild 2
particles to chondrites and IDPs. *Meteoritics &
Planetary Science* 43:261–272.

SUPPORTING INFORMATION

Additional supporting information may be found in
the online version of this article.

Figure S1. a) STEM HAADF image of impactor
residue in crater M1 and EDS maps of b) Mg, c) Si, d)
Fe, e) S, and f) Ni. Large count rates in the protective
Pt cap are the result of Bremsstrahlung radiation.

Figure S2. a) STEM HAADF image of residue on
the wall of crater M1 and EDS maps of b) Mg, c) Si, d)
Fe, e) S, and f) Ca. Large count rates in the protective
Pt cap are the result of Bremsstrahlung radiation.

Figure S3. a) STEM HAADF image of residue on
the floor of crater M2 and EDS maps of b) Mg, c) Si,

d) Fe, e) S, and f) Ni. Large count rates in the
protective Pt cap are the result of Bremsstrahlung
radiation.

Figure S4. a) STEM HAADF image of residue on
the floor of crater M2 and EDS maps of b) Mg, c) Si,
d) Fe, e) S, and f) Ni. Large count rates in the
protective Pt cap are the result of Bremsstrahlung
radiation.

Figure S5. a) STEM HAADF image of residue
from the bulb of residue on the floor of crater M3 and
EDS maps of b) Mg, c) Si, d) Fe,e) S, and f) Ni.

Figure S6. a) STEM HAADF image of residue on
the floor of crater M4 and EDS maps of b) Mg, c) Si,
d) Fe, e) S, and f) Ni.